INTERNATIONAL JOURNAL FOR NUMERICAL METHODS IN FLUIDS
Int. J. Numer. Meth. Fluids 2001; **36**: 125–163

Computing singular solutions of the Navier–Stokes equations with the Chebyshev-collocation method

O. Botella[1] and R. Peyret*,[2]

Laboratoire J.A. Dieudonné, Université de Nice–Sophia Antipolis, Nice, France and INRIA, Sophia Antipolis, France

SUMMARY

The solution of fluid flow problems exhibits a singular behaviour when the conditions imposed on the boundary display some discontinuities or change in type. A treatment of these singularities has to be considered in order to preserve the accuracy of high-order methods, such as spectral methods. The present work concerns the computation of a singular solution of the Navier–Stokes equations using the Chebyshev-collocation method. A singularity subtraction technique is employed, which amounts to computing a smooth solution thanks to the subtraction of the leading part of the singular solution. The latter is determined from an asymptotic expansion of the solution near the singular points. In the case of non-homogeneous boundary conditions, where the leading terms of the expansion are completely determined by the local analysis, the high accuracy of the method is assessed on both steady and unsteady lid-driven cavity flows. An extension of this technique suitable for homogenous boundary conditions is developed for the injection of fluid into a channel. The ability of the method to compute high-Reynolds number flows is demonstrated on a piston-driven two-dimensional flow. Copyright © 2001 John Wiley & Sons, Ltd.

KEY WORDS: asymptotic expansions; Chebyshev-collocation spectral method; Navier–Stokes equations; singular problems

1. INTRODUCTION

The Chebyshev spectral methods are known to be very accurate for smooth solutions: the error is $O(N^{-\gamma})$, where N is the degree of the polynomial and γ is connected to the regularity of the solution. However, in a large number of flows of practical interest, the solution is not smooth and possesses only a small number of continuous derivatives. Even for incompressible flows in

* Correspondence to: Laboratoire J.A. Dieudonné, Université de Nice–Sophia Antipolis, BP 71, Parc Valrose, F-06108 Nice Cedex 2, France.
[1] Current address: Center for Turbulence Research, Building 500, Stanford University, Stanford, CA 94305-3030, U.S.A.
[2] E-mail: peyret@math.unice.fr

Received January 2000
Revised May 2000

a simple rectangular cavity, the solution is not infinitely differentiable. A classical example is given by the existence of an infinite sequence of eddies in a corner with no-slip boundary conditions [1]. In this situation, the second-order derivatives of the vorticity become infinite at the corner. Also, when some of the conditions imposed on the boundary are discontinuous, or change in type, the solution exhibits a singular behaviour that diminishes the accuracy expected from high-order numerical methods such as the Chebyshev method.

These singularities are often introduced by the mathematical modelization of the flow. Let us consider, for example, the flow inside a cylinder chamber, where one of its sides is being compressed under the motion of a piston. Its mathematical modelization introduces singularities at the boundary: more precisely, the velocity of the fluid takes multiple values at the contact points between the moving boundary of the piston and the wall chamber. This modelization leads to a physically unrealistic flow, since by following the analysis of Taylor [2], an infinite force is required to move the piston, and in particular the stress is infinite at the contact points. We may certainly think that, in reality, the piston does not make contact with the wall and there exists a small gap that enables an exchange of fluid between the chamber and the external cylinder. Nonetheless, the fluid leakage must be small enough so that the real-life problem is close to the one modelled. Analogous unrealistic boundary conditions are considered in the driven cavity flow [3] that, in spite of the presence of these singularities, has become one of the reference problems for evaluating numerical methods in fluid dynamics. For this last problem, where the planar motion of fluid in a rectangular cavity is generated by the uniform sliding of one of its walls, the study by Hansen and Kelmanson [4] has justified the validity of the modelization. Even when there is no discontinuities in the boundary conditions or no change in their type, analogous singularities occur at sharp edges of the physical domain. A typical example is given by the flow over a backward-facing step [5], where it is well known that the vorticity becomes unbounded at the re-entrant corner (see, e.g. Reference [1]).

The presence of singularities causes problems in the numerical solution of such flows since the computed solution loses its accuracy in the vicinity of the singular points. Even for 'local' methods, such as the finite difference or finite element methods, spurious oscillations appearing near the singularity may contaminate the solution in the whole domain [6]. This phenomenon is even more acute for global solution methods, such as the Chebyshev method, whose accuracy depends on the regularity of the solution. For a solution with a low regularity, the 'infinite' accuracy commonly associated to spectral methods is lost and such methods show little advantages over local approximation methods. Therefore, a suitable treatment of the singularities is mandatory for preserving, as far as possible, the high accuracy of spectral methods.

Numerous techniques have been proposed for circumventing singularities in fluid flow problems. A first class belongs to *ad hoc* methods, which do not take into account the mathematical structure of the singular solution. A common treatment is to use local grid refinement near the singularity, but the resolution requirement to represent accurately the abrupt change in the solution can be prohibitive. Several methods concerning the imposition of vorticity values in finite difference schemes near re-entrant corner flows are discussed in References [7,8] and references therein. In the framework of spectral methods, it has been proposed to regularize the problem by smoothing the boundary conditions [9], or to use a domain decomposition method to locate the singular point at a corner of the computational domain so that spurious effects are diminished [10].

Most of the other methods require an *a priori* knowledge of the mathematical structure of the singularity. Following the analysis conducted by Moffatt and co-workers [1,11] and Kondrat'ev [12], the solution of the Navier–Stokes equations can be expressed as an asymptotic series which is valid in the near vicinity of the singular point. In the case of homogeneous boundary conditions, the terms of this development are not completely determined by the local analysis but depend on some constants that can only be calculated by considering the global flow. Nevertheless, the knowledge of the leading terms of the expansion can be incorporated in the process of the numerical solution. This idea has led to the development of finite element techniques, where special elements matching the expression of the solution are used near the singular point [6,13,14]. A related approach, based on a singularity adapted interpolation polynomial for generating finite difference approximations has been proposed in Reference [15]. Alternatively, the leading terms can be used to represent the solution in a region surrounding the singular point, the unknown constants being determined by matching the numerical solution computed in the other part of the domain [5,16,17]. Let us also mention that the knowledge of the singular expansion is employed in Reference [8] to improve the derivation of vorticity–streamfunction finite difference scheme for re-entrant corner flows. The efficiency of these methods depends essentially on the validity of the representation of the singular solution by the first terms of the expansion, i.e. only valid at a distance to the singular point inversely proportional to the Reynolds number. Thus, these methods have been essentially applied to flows at moderate values of the Reynolds number.

On the other hand, if the boundary conditions are non-homogeneous, the dominant part of the asymptotic solution is completely determined and this part can then be easily incorporated into the complete solution so that the undetermined part to be computed is more regular. This method, referred to subsequently as the subtraction technique, has been employed in association with Chebyshev methods by Schumack *et al.* [18] for the Stokes flow and by Schultz *et al.* [19] for the Navier–Stokes flow in the driven cavity at low Reynolds numbers. Only the first term of the asymptotic expansion is subtracted in the latter work so that the computed solutions remain weakly singular: the pressure and the vorticity gradient behave respectively, like $\log r$ and r^{-1}, where r is the distance from the singular point.

The purpose of this paper is to employ this technique for the solution of both steady and unsteady singular Navier–Stokes flows, and to shed light on the accuracy of spectral methods for such problems. The association of this technique with the Chebyshev projection scheme introduced in Reference [20] proves to solve accurately a relatively large class of singular Navier–Stokes problems, provided that the leading part of the singular expansion is completely determined. This method is shown to give a high-order convergence rate and is efficiently applied to high-Reynolds number unsteady flows. An extension of the subtraction method is also proposed for the case of homogeneous boundary conditions, where the unknown constants of the singular expansion are determined throughout the solution process. Progress on this work has been reported briefly in Reference [21] and benchmark results on the lid-driven cavity flow obtained with the present method have been presented in Reference [22].

The paper is organized as follows. In Section 2 the accuracy of the Chebyshev-collocation method is investigated on model problems whose singularities mimic ones encountered in the Navier–Stokes applications. In particular, although the 'infinite' order of the Chebyshev method is lost, comparisons with finite difference methods up to sixth order will show that the

accuracy of the spectral method is still superior. Moreover, the convergence rate of the interpolation error for singular functions in two dimensions is numerically established, showing in particular the doubling of the rate for corner singularities. The latter result will prove useful for evaluating the accuracy that is expected when a Chebyshev-collocation scheme is associated with the subtraction technique. A formal technique for the construction of the asymptotic expansion of the singular solution of the unsteady Navier–Stokes equations is presented in Section 3. This technique, an extension of the construction proposed in References [1,11], is applied to a generalization of Taylor's 'scraper problem' [2], where the lid velocity is unsteady. The numerical treatment of singular Navier–Stokes problems is presented in Section 4. The technique of subtraction of the singularity is introduced, and the resulting equations are solved using the projection scheme presented in Reference [20]. The properties of the subtraction technique are first discussed in Section 5 for the driven cavity flow. It is shown in particular that the method gives a global accuracy that agrees with the error estimates obtained in Section 2. The ability of the method to compute flow at high Reynolds number is illustrated by giving results on the unsteady flow at $Re = 9000$. The subtraction method is then applied, in Section 6, to the injection of a fluid into a channel. The discontinuity of the upstream boundary condition introduces singularities whose effects on the spectral solution are worse than in the previous application since they are no longer located at the corners. It will be found necessary to introduce logarithmic terms in the expression of the singular solution, and that the first Navier–Stokes term can only be determined by the local analysis up to a constant. This constant, which depends on the global flow, will be determined numerically by using an iterative process. Finally, computations of the piston-driven flow in a two-dimensional chamber are reported in Section 7. The asymptotic form of the singularities, introduced by the motion of the piston at its contact points with the chamber, is easily derived from the construction described in Section 3. The numerical results show the efficiency of the subtraction method for computing flows of practical interest.

2. THE SPECTRAL ACCURACY

The Chebyshev-collocation method is a global method for solving differential problems. The method consists in approximating the solution with a polynomial of degree N, and requiring that the equation be satisfied at discrete points, which are the extrema of the Chebyshev polynomial T_N. Whereas local methods, such as the finite difference method or the h-version of the finite element method, have a fixed-order of accuracy, the main interest of the Chebyshev-collocation method lies in its properties of accuracy: the method is more accurate as the solution is regular.

For an illustration of this property, let us consider the interpolation of a function u, defined in the one-dimensional domain $\Lambda =]-1, 1[$ by the Chebyshev method. The interpolation polynomial $I_N u$ is defined as the polynomial of degree N which takes the values of u at the $N+1$ Gauss–Lobatto points

$$\Lambda_c = \{x_i = \cos i\pi/N,\ i = 0, \ldots, N\} \tag{1}$$

which are the zeros of the polynomial $(1-x^2)T'_N(x)$. In the framework of Sobolev functional spaces $H^m_w(\Lambda)$, with $m>0$, equipped with the Chebyshev weight $w(x)=(1-x^2)^{-1/2}$, the general theory of interpolation provides the following error estimate, for $u\in H^m_w(\Lambda)$ [23,24]:

$$\|u-I_N u\|_{H^p_w(\Lambda)} \le cN^{p-m}\|u\|_{H^m_w(\Lambda)} \tag{2}$$

where $p=0$ (i.e. the $L^2_w(\Lambda)$ norm) and $p=1$. This error estimate can be qualified as optimal: the power of N appearing in Equation (2) is equal to the difference between the order of the Hilbert spaces appearing in the left and right sides of the inequality. The estimation in the maximum norm $L^\infty(\Lambda)$, which reads

$$\|u-I_N u\|_{L^\infty(\Lambda)} \le cN^{1/2-m}\|u\|_{H^m_w(\Lambda)} \tag{3}$$

will also be considered in the following

If the function u is smooth (i.e. $u\in H^m_w(\Lambda)$ for every $m>0$), Equations (2) and (3) show that the interpolation error decreases more rapidly than any power of $1/N$: it is the well-known exponential accuracy that makes spectral methods so attractive. On the other hand, if u displays a singular behaviour (typically the function possesses only a finite number of continuous derivatives at a singular point $s\in\bar{\Lambda}=[-1,1]$), then the 'infinite' order of accuracy is lost: the general theory shows that the order is algebraic and that it is connected to the regularity of the solution. Furthermore, for applications where the regularity of the solution is weak, the theory shows that the Chebyshev method offers no gain of accuracy against the classical local methods.

Now, the accuracy of the Chebyshev-collocation method is investigated numerically for prototype functions displaying the behaviour $u\sim r^\alpha$ at a singular point $s\in\Lambda$, where r denotes the distance to the point s. The form of these functions is chosen so that it mimics some of the singular solutions of the Navier–Stokes problems considered in the following sections. The precise convergence results that are obtained for the interpolation and the solution of an elliptic equation in this simple one-dimensional setting will prove to be analogous in higher dimensions. These results will give a basis on what accuracy should be expected in the Chebyshev approximation of singular problems.

A typical example of singular function is given by the function u_α defined by

$$u_\alpha(x)=\begin{cases}0, & -1\le x<0\\ x^\alpha, & 0\le x\le 1\end{cases}, \quad \text{with } \alpha>0 \tag{4}$$

The pth derivative of this function, where $\alpha\le p<\alpha+1$, is discontinuous at the middle of the interval Λ; in particular, u_α belongs to $H^m_w(\Lambda)$ for $m<\alpha+1/2$. By denoting $\mathscr{I}_N=u_\alpha-I_N u_\alpha$, Equations (2) and (3) give the following theoretical convergence rates:

$$\|\mathscr{I}_N\|_{L^2_w(\Lambda)}\le c_1N^{-1/2-\alpha}, \qquad \|\mathscr{I}_N\|_{L^\infty(\Lambda)}\le c_2N^{-\alpha}, \qquad \|\mathscr{I}_N\|_{H^1_w(\Lambda)}\le c_3N^{1/2-\alpha} \tag{5}$$

Table I. Order of the interpolation error of the singular function $u_\alpha(x)$ (Equation (4)), evaluated numerically for various norms.

	$\alpha = 2$	$\alpha = 4$	$\alpha = 6$
$L^2_w(\Lambda)$	2.5	4.5	6.5
$L^\infty(\Lambda)$	2.0	4.0	6.1
$H^1_w(\Lambda)$	1.5	3.5	5.6

were c_1, c_2, c_3 are positive constants related to the norm of u_α. Table I displays the numerical estimation of the convergence rate γ obtained for the interpolation of u_α, for $\alpha = 2$, 4 and 6. The value of γ is estimated by considering interpolation polynomials of degree N in the range [8, 24]. The continuous $L^2_w(\Lambda)$ and $H^1_w(\Lambda)$ norms are calculated by evaluating the value of $I_N u_\alpha$ and $(I_N u_\alpha)'$ on the $M+1$ Gauss–Lobatto grid, with $M = 1000$, and by using the Gauss–Lobatto quadrature formula. The $L^\infty(\Lambda)$ norm is approximated by taking the maximum of I_N on the above $M+1$ points. The results displayed in Table I show that, for this singular function, the numerical convergence rates match the theoretical ones given by Equation (5).

The second example deals with the function v_α, defined in Λ by

$$v_\alpha(x) = (1 - x^2)^\alpha \tag{6}$$

where $\alpha > 0$ is not an integer and whose singularity no longer lies in the interior of Λ but at its boundary. More precisely, the function v_α belongs to $H^m_w(\Lambda)$ for every $m < \alpha + 1/4$. The following theoretical convergence rates are deduced from Equations (2) and (3):

$$\|\mathscr{I}_N\|_{L^2_w(\Lambda)} \leq c_1 N^{-1/4-\alpha}, \qquad \|\mathscr{I}_N\|_{L^\infty(\Lambda)} \leq c_2 N^{1/4-\alpha}, \qquad \|\mathscr{I}_N\|_{H^1_w(\Lambda)} \leq c_3 N^{3/4-\alpha} \tag{7}$$

For diverse values of α, Table II display the convergence rates of the interpolation of v_α, estimated numerically by the same method as described above. One can infer from these results that the estimated rate is much larger than the one predicted by the general theory (Equation (7)) and that the interpolation error follows, in fact, the rule:

$$\|\mathscr{I}_N\|_{L^2_w(\Lambda)} = O(N^{-1/2-2\alpha}), \qquad \|\mathscr{I}_N\|_{L^\infty(\Lambda)} = O(N^{-2\alpha}), \qquad \|\mathscr{I}_N\|_{H^1_w(\Lambda)} = O(N^{3/2-\alpha}) \tag{8}$$

In particular, in the Hilbertian norms, $L^2_w(\Lambda)$ and $H^1_w(\Lambda)$, the order of accuracy is exactly twice the rate given in Equation (7). We have to mention that these numerical results concerning the

Table II. Order of the interpolation error of the singular function $v_\alpha(x)$ (Equation (6)), evaluated numerically for various norms.

	$\alpha = 0.9$	$\alpha = 1.9$	$\alpha = 2.9$
$L^2_w(\Lambda)$	2.2	4.2	6.2
$L^\infty(\Lambda)$	1.8	3.8	5.9
$H^1_w(\Lambda)$	0.3	2.3	4.4

doubling of the convergence rate are in accordance with the theoretical results established by Bernardi and Maday [25] for approximations by Jacobi polynomials (with the weight $w(x) = (1-x)^{-1/2}$).

Then, let us consider the approximation of the one-dimensional Dirichlet problem

$$Lu(x) = f(x), \quad x \in \Lambda \tag{9a}$$

$$u(-1) = g_0, \qquad u(1) = g_1 \tag{9b}$$

where L is a second-order elliptic operator. For the Poisson equation ($L = -\mathrm{d}^2/\mathrm{d}x^2$), the collocation solution u_N of Equation (9) verifies the optimal error estimate for $u \in H_w^m(\Lambda)$ and $f \in H_w^{m-1}(\Lambda)$ with $m \geq 2$ [26]

$$\|u - u_N\|_{H_w^1(\Lambda)} \leq cN^{1-m}(\|u\|_{H_w^m(\Lambda)} + \|f\|_{H_w^{m-1}(\Lambda)}) \tag{10}$$

As in the interpolation case, this estimate shows that the accuracy of the spectral solution is governed by the regularity of the solution. As an illustration of this property (Figure 1), let us compare the accuracy of the solution of Equation (9) with $L = \lambda^2 - \mathrm{d}^2/\mathrm{d}x^2$, $\lambda = 10$, obtained using various methods: second-order finite difference method, uniform grid $h = 2/N$ (curve 1) and Gauss–Lobatto grid (1) (curve 2); sixth-order Hermitian method with uniform grid [27] (curve 3) and Gauss–Lobatto grid (1) [28] (curve 4); and, finally, Chebyshev-collocation method with Gauss–Lobatto grid (1) (curve 5). The error E is measured with the discrete $l^2(\Lambda)$ norm defined by

$$E = \left(\frac{1}{N-1} \sum_{i=1}^{N-1} |u(x_i) - u_N(x_i)|^2 \right)^{1/2} \tag{11}$$

where u refers to the exact solution. Figure 1(a) displays the error E for the smooth solution

$$u(x) = 1 - \frac{\sinh \lambda(x+1)}{\sinh 2\lambda} \tag{12}$$

obtained for $f = \lambda^2$, $g_0 = 1$, $g_1 = 0$. According to the general theory, which provides an error estimate analogous to Equation (10) for this problem [29], the spectral solution exhibits an exponential convergence rate. The second example (Figure 1(b)) concerns the calculation of the singular solution (6) with $\alpha = 2.9$, from which we define f in Equation (9a) and $g_0 = g_1 = 0$. The convergence rate observed for this solution, and for other values of α, is given in Table III for the various methods. It can be seen in Figure 1(b) that not only is the accuracy of the spectral method but also that of the high-order Hermitian methods affected by the singularity. The Hermitian method with the collocation mesh takes advantage of the clustering of the

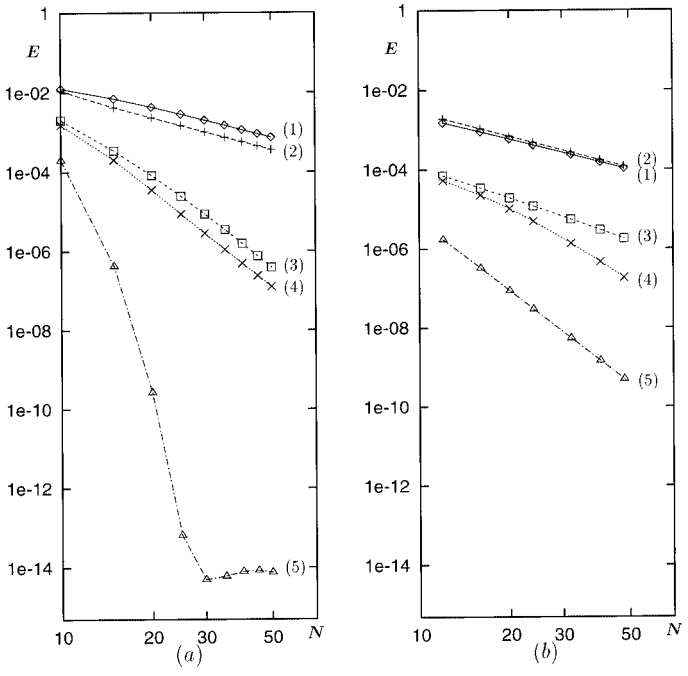

Figure 1. Error E versus the number N of degrees of freedom: (a) smooth solution, (b) singular solution (see the text for the meaning of the labels).

Gauss–Lobatto points near the boundary, where $h \sim 1/N^2$, which leads to an improvement of the convergence rate compared with the equal-order scheme with uniform mesh. Nevertheless, the spectral method proves to be the scheme that gives the lowest magnitude error for these types of singularities. Moreover, it has been checked for this example that the convergence rate of the spectral approximation in the continuous norms $L^2_w(\Lambda)$, $L^\infty(\Lambda)$ and $H^1_w(\Lambda)$ matches

Table III. Order of the error E obtained for the solution of problem (9) with the singular solution (6) using finite difference methods and the Chebyshev-collocation method.

	Finite difference, second-order		Finite difference, sixth-order		Chebyshev-collocation
	Uniform mesh	Gauss–Lobatto	Uniform mesh	Gauss–Lobatto	
$\alpha = 2.1$	1.8	2.0	2.1	4.2	4.7
$\alpha = 2.9$	2.0	2.0	2.9	5.6	5.9
$\alpha = 3.1$	2.0	2.0	3.1	5.9	6.3
$\alpha = 4.9$	2.0	2.0	5.2	6.0	10.5

those displayed in Table II for the interpolation case. Thus, we can infer that the Chebyshev-collocation error of the Helmholtz problem (9), whose singular solution is Equation (6), is optimal and follows the rules:

$$\|u-u_N\|_{L^2_w(\Lambda)} = O(N^{-1/2-2\alpha}), \qquad \|u-u_N\|_{L^\infty(\Lambda)} = O(N^{-2\alpha})$$

$$\|u-u_N\|_{H^1_w(\Lambda)} = O(N^{3/2-2\alpha}) \tag{13}$$

Finally, we propose to evaluate the interpolation error of the singular functions involved in the asymptotic solution of the two-dimensional Navier–Stokes problems considered in following sections. In the domain $\Omega =]-1, 1[^2$, the singular functions take the form

$$u^s_{\alpha,\beta} = r^\alpha \log r^\beta f(\theta), \quad \text{with } \alpha \geq 1, \quad \beta = 0 \text{ or } 1 \tag{14}$$

in the polar co-ordinate system (r, θ) centred at the singular point $s \in \partial\Omega$, where $f(\theta)$ is smooth function. For the flow in the driven cavity and in the piston engine, the point s is located at the corners of the domain (the functions $u^s_{\alpha,\beta}$ are then typical corner singularities), while in the injection problem, the point s is located on the edge of Ω. For the first two applications only functions of the form $r^\alpha f(\theta)$ are involved in the asymptotic solution. However, logarithmic terms can be present in the asymptotic solution of singular Navier–Stokes problems (Kondrat'ev [12]) such as the injection problem. As a matter of fact, the interpolation error of $u^s_{\alpha,\beta}$ is evaluated in two distinct cases. At first the point s is located at $(-1, 1/2)$ in the middle of an edge of Ω, and the function f reads

$$f(\theta) = \frac{Re}{16\pi^2}\left\{(\pi-\theta)\cos\theta + 2\left(\theta^2 - \pi\theta + \frac{21}{8}\right)\sin\theta + (\theta-\pi)\cos 3\theta - \frac{7}{4}\sin 3\theta\right\} \tag{15}$$

with $Re = 1000$. This function is found in the second term of the singular expansion of the velocity in the injection problem. In a second case, the point s is at the corner $(-1, 1)$ of Ω. The function f is now given by the term $u_2^A(\theta; Re)$, with $Re = 1000$, which is involved in the asymptotic solution of the driven cavity flow; its expression can be found in the appendix of Reference [22]. We recall that the general theory of interpolation provides an error estimate in the $L^2_w(\Omega)$ norm similar to Equation (2) for the one-dimensional case [23,26].

Table IV displays the numerical estimation of the rate of the interpolation error $\|u^s_{\alpha,\beta} - I_N u^s_{\alpha,\beta}\|_{L^2_w(\Omega)}$ obtained for various values of (α, β); the $L^2_w(\Omega)$ norm has been evaluated using

Table IV. Order of the interpolation error of the two-dimensional function $u^s_{\alpha,\beta}$, for various location of the singular point s.

s	r^3	$r^3 \log r$	r^2	$r^2 \log r$	r	$r \log r$
$(-1, 1/2)$	3.70	3.59	2.75	2.55	1.75	1.54
$(-1, 1)$	6.9	6.6	4.9	4.6	3.0	2.7

the Gauss–Lobato quadrature formula with $M = 800$ in both directions. Firstly, it can be inferred from the results of Table IV that when s is in the middle of an edge, the interpolation rate follows:

$$\left\| u^s_{\alpha,0} - I_N u^s_{\alpha,0} \right\|_{L^2_w(\Omega)} = O(N^{-3/4-\alpha}) \tag{16}$$

and when s is located at a corner

$$\left\| u^s_{\alpha,0} - I_N u^s_{\alpha,0} \right\|_{L^2_w(\Omega)} = O(N^{-1-2\alpha}) \tag{17}$$

Secondly, the presence of the logarithmic term only has slight influence on the convergence rate, i.e. the interpolation error of $u^s_{\alpha,0}$ and $u^s_{\alpha,1}$ depends essentially on α.

The comparison between Equations (16) and (17) shows that the convergence rate for corner singularities is essentially twice better than for edge singularities, up to a constant induced by the Chebyshev weight. This doubling of the rate has already been noticed in References [25,30,31] for the spectral Legendre, spectral element and h–p finite element methods respectively. Estimates (16) and (17) will prove useful for the evaluation of the singularity subtraction method, which is applied to the Navier–Stokes equations in Section 4 and subsequent sections.

3. SINGULAR SOLUTIONS OF THE NAVIER–STOKES EQUATIONS

In the task of computing unsteady singular solutions of the Navier–Stokes equations by using the subtraction method, we describe in the present section the technique for determining the asymptotic expansion near a singular point, in a situation where the flow may depend on time. The model problem is chosen as the flow of a viscous fluid near the contact point s between two perpendicular walls, where the motion is generated by the sliding of one of the walls in its own plane with a given velocity (see Figure 2). This configuration generalizes the steady 'scraper problem' of Taylor [2,32] with a lid velocity that is now supposed to be a function of the time. This problem is somewhat academic but it retains the characteristic features of the singular solutions of both the driven cavity and the piston engine problems discussed in the following sections.

The flow is governed by the two-dimensional Navier–stokes equations for an incompressible fluid where $\boldsymbol{V} = (u, v)$ is the velocity vector, p is the pressure; the Reynolds number Re is defined by the viscosity of the fluid, a characteristic value of the wall velocity (e.g. its maximum) and a length L, which is arbitrary for this problem. The boundary conditions are $\boldsymbol{V} = (U(t), 0)$ on the sliding wall and $\boldsymbol{V} = \boldsymbol{0}$ on the stationary wall. The initial condition is the rest, the velocity of the lid $U(t)$ being equal to zero at the initial time. Let us note that the asymptotic expansion constructed hereafter may only be valid after a short time away from $t = 0$. A description of the singular solution up to the initial time that is legitimate for a general

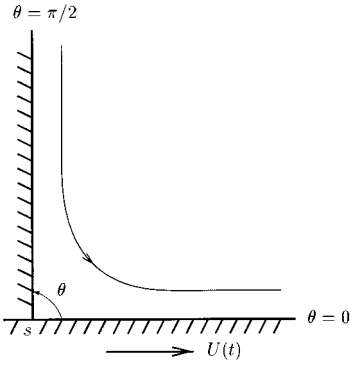

Figure 2. Sketch of the scraper problem with an unsteady velocity $U(t)$.

form of $U(t)$ would require the matching with additional transient terms so that the initial condition is satisfied; such a construction is out of the scope of the utilization of the subtraction method. On the other hand, we will discuss conditions on the derivatives of $U(t)$ at $t = 0$, which may be necessary for using the leading terms of the singular solution in the numerical technique described in the next section.

Due to the discontinuity of the boundary conditions at the corner s, the solution of the Navier–Stokes equations is not infinitely differentiable. For determining the asymptotic solution near the singular point s, it is convenient to introduce the streamfunction ψ (such that $u = \partial\psi/\partial y$, $v = -\partial\psi/\partial x$) and to consider a local co-ordinate system (r, θ) defined by $x = x_s + r\cos\theta$, $y = y_s + r\sin\theta$, where (x_s, y_s) corresponds to the fixed point s and r is the distance to this point. The equation satisfied by the streamfunction is

$$\nabla^4\psi = Re\left[\frac{\partial\nabla^2\psi}{\partial t} + \boldsymbol{V}\cdot\nabla(\nabla^2\psi)\right] \tag{18}$$

the associated boundary conditions are

$$\frac{\partial\psi}{\partial r} = 0, \qquad \frac{1}{r}\frac{\partial\psi}{\partial\theta} = U(t) \quad \text{on } \theta = 0; \qquad \frac{\partial\psi}{\partial r} = 0, \quad \frac{1}{r}\frac{\partial\psi}{\partial\theta} = 0 \quad \text{on } \theta = \frac{\pi}{2} \tag{19}$$

In the neighbourhood of the point s, the singular solution of Equation (18) can be written as the asymptotic expansion

$$\psi = \sum_{k\geq 1}\psi_k \quad \text{with } \psi_k = r^{\alpha_k} f_k(\theta, t) \tag{20}$$

where the functions f_k are smooth. The exponents α_k, which can be complex, are such that each term in Equation (20) is less singular than the previous one, i.e.

$$1 \leq Re(\alpha_1) < Re(\alpha_2) < \cdots \tag{21}$$

In previous works [1,11,33] it was assumed that in the steady state case, the flow near the corner s was dominated by viscous forces, so that the first term ψ_1 is a solution to the Stokes system. The following terms were obtained either as corrective terms generated by inertia forces [11] or as a power series in Re [33]. Both methods do not take into account in their asymptotic solution the contribution of the eigenfunctions of the Stokes system [1]. The expression of these eigenfunctions is $\psi_\lambda = r^\lambda f$, where λ is any complex number solution to

$$\sin(\lambda - 1)\theta = \pm(\lambda - 1)\sin\theta \tag{22}$$

with $\theta = \pi/2$, and f is determined up to a scalar function $K_\lambda(t)$ of the time. In the following we shall describe a technique for the determination of the first and most singular terms of Equation (20). This formal technique does not require additional assumptions on the value of the Reynolds number and allows the eigenfunctions to be introduced in a systematic way.

First, the substitution of expansion (20) into Equation (18) yields

$$\sum_{k \geq 1} r^{\alpha_k} \mathscr{L}_{\alpha_k} f_k = Re\left[\sum_{k \geq 1} r^{2+\alpha_k} \mathscr{T}_{\alpha_k} \dot{f}_k + \sum_{i,j \geq 1} r^{\alpha_i + \alpha_j} \mathscr{N}_{\alpha_i,\alpha_j}(f_i, f_j) \right] \tag{23}$$

where $\dot{f}_k$ refers to the derivative with respect to t, and $\mathscr{L}_{\alpha_k}$, $\mathscr{T}_{\alpha_k}$ and $\mathscr{N}_{\alpha_i,\alpha_j}$ are differential operators with respect to θ, respectively defined by

$$\mathscr{L}_{\alpha_k} f_k = f_k^{iv} + [(\alpha_k - 2)^2 + \alpha_k^2] f_k'' + \alpha_k^2 (\alpha_k - 2)^2 f_k \tag{24a}$$

$$\mathscr{T}_{\alpha_k} f_k = \alpha_k^2 f_k + f_k'' \tag{24b}$$

$$\mathscr{N}_{\alpha_i,\alpha_j}(f_i, f_j) = (\alpha_j - 2) f_1' \mathscr{T}_{\alpha_j} f_j - \alpha_i f_i \mathscr{T}_{\alpha_j} f_j' \tag{24c}$$

The associated boundary conditions obtained from Equation (19) read, for $k = 1$

$$f_1(0) = 0, \qquad r^{\alpha_1 - 1} f_1'(0) = U(t), \qquad f_1(\pi/2) = 0, \qquad f_1'(\pi/2) = 0 \tag{25}$$

and for $k \geq 2$, the functions f_k admit the homogeneous boundary conditions

$$f_k(0) = 0, \qquad f_k'(0) = 0, \qquad f_k(\pi/2) = 0, \qquad f_k'(\pi/2) = 0 \tag{26}$$

Every term of expansion (20) is obtained by cancelling the terms of equal power in expression (23). Starting from the one with the lowest exponent (i.e. the most singular), each term is then successively deduced from the previous ones. First, we have to arrange, as far as possible, each side of Equation (23) in increasing order of the real part of the exponent. The first term of the left-hand side of Equarion (23) is in r^{α_1} and, without knowing the value of α_1, it is not possible to determine whether the dominant term of the right-hand side is in $r^{2+\alpha_1}$ or in $r^{2\alpha_1}$. However, whatever the relative order of these last two terms, the most singular part in

Equation (23) is the term in r^{α_1} and the cancellation of this term leads to the differential equation

$$\mathscr{L}_{\alpha_1} f_1 = 0 \tag{27}$$

with the non-homogeneous boundary conditions (25). The second of these conditions leads to $\alpha_1 = 1$, the function f_1 is then completely determined and is proportional to $U(t)$; its expression can be found, for example, in References [1,22]. Note that Equation (27) shows that $\psi_1 = rf_1$ is a solution to the Stokes equation $\mathbf{\nabla}^4\psi_1 = 0$, the time appearing only as a parameter.

Since the term in r^{α_1} is cancelled, Equation (23) becomes

$$r^{\alpha_2}\mathscr{L}_{\alpha_2} f_2 + r^{\alpha_3}\mathscr{L}_{\alpha_3} f_3 + \cdots = r^2 Re\,\mathscr{N}_{1,1}(f_1, f_1) + \cdots \tag{28}$$

the following term on the right-hand side being in r^3 and/or in $r^{1+\alpha_2}$, depending on the value of α_2, yet unknown. Let us compare the magnitude of the exponent of the first term in each side of Equation (28), i.e. α_2 and 2. The expression $\mathscr{N}_{1,1}(f_1, f_1)$ is a non-vanishing term depending only on f_1 (i.e. independent of r), thus $Re(\alpha_2) \leq 2$. If $Re(\alpha_2) < 2$, then f_2 would be a solution to $\mathscr{L}_{\alpha_2} f_2 = 0$ with the homogeneous boundary conditions (26), i.e. ψ_2 would be an eigenfunction of the Stokes problem and α_2 should be identified with the first root λ_1 of Equation (22). This case is impossible since the root with the smallest real part is (Reference [1]):

$$\lambda_1 \simeq 3.74 + 1.13\underline{i} \tag{29}$$

Thus α_2 is necessarily equal to 2 and f_2 is completely determined by the differential equation

$$\mathscr{L}_2 f_2 = Re\,\mathscr{N}_{1,1}(f_1, f_1) \tag{30}$$

with the homogeneous boundary conditions (26). This implies that $\psi_2 = r^2 f_2$ is generated by the inertia forces of the Navier–Stokes equations, and this term is found to be proportional to $ReU^2(t)$. Its expression is given in, e.g. References [11,22].

This algorithm can be employed for the determination of the successive terms of the singular expansion (20). The cancellation of the following terms of Equation (23) gives $\alpha_3 = 3$ and leads to the differential equation for f_3

$$\mathscr{L}_3 f_3 = Re[\mathscr{T}_1 \dot{f}_1 + \mathscr{N}_{1,2}(f_1, f_2) + \mathscr{N}_{2,1}(f_2, f_1)] \tag{31}$$

with the homogeneous boundary conditions (26). Thus, the singular term $\psi_3 = r^3 f_3$ is generated by both unsteady and inertia forces of the Navier–Stokes equations. This term is completely determined by Equations (31) and (26) and is proportional to Re^2, with one part proportional to $U(t)$ and another one to $U^3(t)$. The following term, ψ_4, is found to be an eigenfunction of the Stokes system of the form $\psi_4 = r^{\lambda_1} f_4$, where $\lambda_1 = p_1 + \underline{i}q_1$ is given by Equation (29), that can be written as

$$\psi_4 = K_{\lambda_1}(t) r^{p_1}[\cos(q_1 \log r) g_5(\theta) + \sin(q_1 \log r) h_5(\theta)] \tag{32}$$

where the function $K_{\lambda_1}(t)$ is undetermined by this local analysis and has to be calculated by considering the global flow.

In this fashion, it is possible to build the first terms of the asymptotic solution of the Navier–Stokes equation near the point s

$$\psi = rf_1(\theta, t) + r^2 f_2(\theta, t) + r^3 f_3(\theta, t) + r^{\lambda_1} f_4(\theta, t) + r^4 f_5(\theta, t) + r^{1+\lambda_1} f_6(\theta, t) + o(r^{1+\lambda_1}) \tag{33}$$

As stated previously, this asymptotic solution may not be correct at $t = 0$ when the lid velocity $U(t)$ varies with time. Only the first two terms will be used in the examples reported hereafter, and they represent a valid approximation of the singular solution at $t = 0$ provided that $U(0) = 0$. On the other hand, note that $\psi_3 = r^3 f_3$ is proportional to $\dot{U}(t) + U^3(t)$. The consideration of this term for representing the third singular term at the initial time would furthermore require that $\dot{U}(0) = 0$.

4. NUMERICAL TREATMENT

The principle of the subtraction technique is to calculate a sufficiently smooth solution thanks to the subtraction of the leading part of the singular solution. In the case of singular problems, such as the scraper problem, where the boundary conditions are non-homogeneous and the first terms of the asymptotic solution near the singular point s are completely determined from the local analysis, these singular terms can be easily subtracted from the complete solution according to

$$\boldsymbol{V} = \tilde{\boldsymbol{V}} + \bar{\boldsymbol{V}}, \qquad p = \tilde{p} + \bar{p} \tag{34}$$

The field $(\tilde{\boldsymbol{V}}, \tilde{p})$ refers to the first K terms of the asymptotic solution

$$\tilde{\boldsymbol{V}} = \sum_{k=1}^{K} \boldsymbol{V}_k, \qquad \tilde{p} = \sum_{k=1}^{K} p_k \tag{35}$$

where $(\boldsymbol{V}_k, p_k)$ is calculated from ψ_k defined in Equation (20). The resulting field $(\bar{\boldsymbol{V}}, \bar{p})$ is more regular than $(\boldsymbol{V}, p)$, since its behaviour near the singular points is given by the first term of the asymptotic solution neglected in Equation (35), i.e.

$$\bar{\boldsymbol{V}} \sim \boldsymbol{V}_{K+1}, \qquad \bar{p} \sim p_{K+1} \tag{36}$$

The field $(\bar{\boldsymbol{V}}, \bar{p})$ satisfies the set of equations

$$\frac{\partial \bar{\boldsymbol{V}}}{\partial t} + \mathcal{N}(\bar{\boldsymbol{V}}, \tilde{\boldsymbol{V}}) - \frac{1}{Re} \nabla^2 \bar{\boldsymbol{V}} + \nabla \bar{p} = \mathscr{F} \tag{37a}$$

$$\nabla \cdot \bar{\boldsymbol{V}} = 0 \tag{37b}$$

which is similar to the Navier–Stokes system where

$$\mathcal{N}(\bar{\boldsymbol{V}}, \tilde{\boldsymbol{V}}) = (\bar{\boldsymbol{V}}\cdot\boldsymbol{\nabla})\bar{\boldsymbol{V}} + (\tilde{\boldsymbol{V}}\cdot\boldsymbol{\nabla})\bar{\boldsymbol{V}} + (\bar{\boldsymbol{V}}\cdot\boldsymbol{\nabla})\tilde{\boldsymbol{V}} \tag{38}$$

and $\mathscr{F}$ is a source term depending only on $\tilde{\boldsymbol{V}}$. These equations are solved in the bounded domain Ω, and the associated boundary conditions

$$\bar{\boldsymbol{V}} = \mathbf{g} \quad \text{on } \partial\Omega \tag{39}$$

where $\mathbf{g}$ (which depends also on $\tilde{\boldsymbol{V}}$) has a zero total flux through $\partial\Omega$. The initial condition $\bar{\boldsymbol{V}}^0 = \boldsymbol{V}(0) - \tilde{\boldsymbol{V}}(0)$ is defined as a square integrable function verifying the incompressibility constraint (37b) such that

$$\bar{\boldsymbol{V}}^0\cdot\mathbf{n} = \mathbf{g}^0\cdot\mathbf{n} \quad \text{on } \partial\Omega \tag{40}$$

In the examples reported hereafter, it has been proved sufficient to subtract the first two terms of the asymptotic solution ($K = 2$, NS2 solution technique) to obtain excellent convergence properties. Calculations where only the first term is removed or where no singular terms are removed were also considered and referred to in the following as the NS1 technique and the NS0 technique respectively.

Equations (37)–(39) are solved by means of the projection schemes developed by Botella [20,28] and defined by the two following steps:

- Prediction step

$$\frac{1}{\Delta t}\left(a_0\bar{\boldsymbol{V}}^* + \sum_{i=0}^{2} b_i\bar{\boldsymbol{V}}^{n-i}\right) + \sum_{i=0}^{2} d_i\mathcal{N}(\bar{\boldsymbol{V}}^{n-i}, \tilde{\boldsymbol{V}}^{n+1}) - \frac{1}{Re}\boldsymbol{\nabla}^2\bar{\boldsymbol{V}}^* + \sum_{i=0}^{1} c_i\boldsymbol{\nabla}\bar{p}^{n-i} = \mathscr{F}^{n+1} \tag{41a}$$

$$\bar{\boldsymbol{V}}^*_{|\partial\Omega} = \mathbf{g}^{n+1} \tag{41b}$$

- Projection step

$$\frac{a_0}{\Delta t}(\bar{\boldsymbol{V}}^{n+1} - \bar{\boldsymbol{V}}^*) + \boldsymbol{\nabla}\left(\bar{p}^n - \sum_{i=0}^{1} c_i\bar{p}^{n-i}\right) = 0 \tag{42a}$$

$$\boldsymbol{\nabla}\cdot\bar{\boldsymbol{V}}^{n+1} = 0 \tag{42b}$$

$$\bar{\boldsymbol{V}}^{n+1}\cdot\mathbf{n}_{|\partial\Omega} = \mathbf{g}^{n+1}\cdot\mathbf{n} \tag{42c}$$

where Δt denotes the time step and the superscript n indicates that the variables are evaluated at the time $t = n\Delta t$ for $n = 0, 1, 2, \ldots$ These schemes combine a backward time differentiation formula, an Adams–Bashforth extrapolation for the convective term and a semi-implicit extrapolation for the pressure. The a_0, b_i, c_i, d_i coefficients, yielding second-order and

Table V. Coefficients of the second- and third-order projection schemes.

Order	a_0	b_0	b_1	b_2	c_0	c_1	d_0	d_1	d_2
2	3/2	−2	1/2	0	1	0	2	−1	0
3	11/6	−3	3/2	−1/3	2	−1	3	−3	1

third-order time accurate schemes, are given in Table V. The third-order scheme has been employed for the unsteady computations reported hereafter, while steady states computations were obtained by means of the second-order scheme. In the latter case, the steady solution is defined by

$$\frac{\max_{\bar{\Omega}_c} |\phi^{n+1} - \phi^n|}{\Delta t \max_{\bar{\Omega}_c} |\phi^{n+1}|} \leq \epsilon \tag{43}$$

were ϕ denotes the components of $\bar{V}$ and $\bar{\Omega}_c$ refers to the computational grid. The values of ϵ will be defined for each of the examples reported below.

The special approximation is based on a $\mathbb{P}_N - \mathbb{P}_{N-2}$ Chebyshev-collocation method, where the velocity is approximated with a polynomial of degree N_x at most in the x-direction and N_y in the y-direction, its values being defined on the $(N_x+1) \times (N_y+1)$ Gauss–Lobatto grid. On the other hand, the pressure is defined as a polynomial of degree two less in both directions, and is calculated at the inner nodes of the above Gauss–Lobatto grid. The prediction step (41) amounts to a Helmholtz problem for $\bar{V}^*$ solved by means of the diagonalization method [34]. The projection step (42) is discretized such that the divergence equation is satisfied at the inner collocation nodes (strong formulation, Botella [20]) and results in an Uzawa equation for the pressure, solved by the diagonalization technique. This discretization prevents the pressure from being polluted by spurious modes, and avoids the necessity to prescribe boundary conditions for the pressure. This way of solving the projection step enables us to build high-order projection schemes, where the order of the time accuracy of the velocity and of the pressure is the same.

When using a multi-step scheme, the usual problem is to calculate the solution at the first time cycles, namely $(\bar{V}^1, \bar{p}^1)$ for the second-order scheme and $(\bar{V}^1, \bar{p}^1)$ and $(\bar{V}^2, \bar{p}^2)$ for the third-order one. The second-order scheme is used here only for the calculation of steady solutions, so that the accuracy of the starting scheme is not of importance. Therefore, we simply pose $\bar{V}^{-1} = \bar{V}^0$ and $\bar{p}^0 = 0$, which leads, with a convenient value of Δt, to a first-order scheme. For the computations using the third-order scheme, the calculations of $(\bar{V}^1, \bar{p}^1)$ and $(\bar{V}^2, \bar{p}^2)$ are performed by using the following starting scheme of implicit Runge–Kutta type:

$$\frac{\bar{V}^* - \bar{V}^n}{\Delta t} + \mathcal{N}(\bar{V}^n, \tilde{V}^n) - \frac{1}{Re} \nabla^2 \bar{V}^n + \nabla \bar{p}^n = \mathcal{F}^n \tag{44a}$$

$$\bar{V}^*_{|\partial\Omega} = \mathbf{g}^{n+1} \tag{44b}$$

$$\frac{2\bar{\boldsymbol{V}}^{**} - \bar{\boldsymbol{V}}^{*} - \bar{\boldsymbol{V}}^{n}}{\Delta t} + \mathcal{N}(\bar{\boldsymbol{V}}^{*}, \tilde{\boldsymbol{V}}^{n+1}) - \frac{1}{Re}\nabla^2 \bar{\boldsymbol{V}}^{**} + \nabla \bar{p}^{n} = \mathscr{F}^{n+1} \tag{45a}$$

$$\bar{\boldsymbol{V}}^{**}_{|\partial\Omega} = \mathbf{g}^{n+1} \tag{45b}$$

$$\frac{\bar{\boldsymbol{V}}^{n+1} - \bar{\boldsymbol{V}}^{**}}{\Delta t} + \frac{1}{2}\nabla(\bar{p}^{n+1} - \bar{p}^{n}) = 0 \tag{46a}$$

$$\nabla \cdot \bar{\boldsymbol{V}}^{n+1} = 0 \tag{46b}$$

$$\bar{\boldsymbol{V}}^{n+1} \cdot \mathbf{n}_{|\partial\Omega} = \mathbf{g}^{n+1} \cdot \mathbf{n} \tag{46c}$$

The truncation error of this scheme is of second-order but according to classical results on the accuracy of solution of ordinary differential equations [35], the solution $(\bar{\boldsymbol{V}}^{n}, \bar{p}^{n})$ for $n = 0, 1$ is expected to be third-order accurate. In addition to the initial condition $\bar{\boldsymbol{V}}^{0}$, the scheme needs the knowledge of an initial pressure field $\bar{p}^{0}$. This pressure field is determined from the Neumann problem [36,37]

$$\nabla^2 \bar{p}^{0} = \nabla \cdot [\mathscr{F}^{0} - \mathcal{N}(\bar{\boldsymbol{V}}^{0}, \tilde{\boldsymbol{V}}^{0})] \quad \text{in } \Omega \tag{47a}$$

$$\frac{\partial \bar{p}^{0}}{\partial \mathbf{n}} = \left[\mathscr{F}^{0} + \frac{1}{Re}\nabla^2 \bar{\boldsymbol{V}}^{0} - \mathcal{N}(\bar{\boldsymbol{V}}^{0}, \tilde{\boldsymbol{V}}^{0}) - \frac{\partial \bar{\boldsymbol{V}}^{0}}{\partial t}\right] \cdot \mathbf{n} \quad \text{on } \partial\Omega \tag{47b}$$

These equations are obtained by taking at $t = 0$ the divergence of Equation (37a) and its normal component at the boundary respectively. Note that the solution at subsequent times may display a singular behaviour near $t = 0$ if some compatibility conditions on the data are not satisfied [36–38]. This is not a consequence of the determination of $\bar{p}^{0}$ but a general result on the regularity of the solution of the Navier–Stokes equations near $t = 0$. However, from the computational point of view, the effect of such a singularity is rapidly damped.

5. LID-DRIVEN CAVITY FLOW

The first example of the application of the subtraction technique to the solution of singular Navier–Stokes problems concerns the well-known lid-driven cavity flow, to be solved in the domain $\Omega =]0, 1[\times]0, 1[$. The boundary conditions are $\boldsymbol{V} = (-1, 0)$ on the side $y = 1$ and $\boldsymbol{V} = 0$ on the other three sides. The reference quantities for this problem are the top-wall velocity and the length of the side of the square.

The main difficulty of the numerical solution of this problem is, at least for spectral methods, the presence of singularities at the corners. At corners $s = A(0, 1)$ and $s = B(1, 1)$, where the velocity is discontinuous, the local singular solution can be written as the asymptotic expansion (20), whose first terms read

$$\psi^{s} = r f_1^{s}(\theta) + r^2 f_2^{s}(\theta) + r^3 f_3^{s}(\theta) + r^{\lambda_1} f_4^{s}(\theta, t) + \cdots \tag{48}$$

The first three terms are completely determined by the algorithm described in Section 3, and since the boundary conditions are stationary, they are found independent of time. The analytic expression of $\psi_1^s = rf_1^s$ and $\psi_2^s = r^2 f_2^s$, which are to be used in the subtraction method, are given by Botella and Peyret [22]. The first term ψ_1^s characterizes the behaviour of the solution near the singular corners: at $s = A$, B the vorticity $\omega = \partial v/\partial x - \partial u/\partial y$ and the pressure are infinite and behave like $1/r$. On the other hand, at corners $C(1, 0)$ and $D(0, 0)$, where the boundary conditions are homogeneous, the leading term of the expansion is given by the first eigenfunction (32) of the Stokes problem, so that the singularity is much weaker since only the second derivatives of ω and p are unbounded. As we shall see later, the effects of this singularity is relatively weak on the numerical solution and its treatment is not taken into account in this work.

For this problem, the subtraction method consists in decomposing the field $(\boldsymbol{V}, p)$ according to Equation (34), where the singular part $(\tilde{\boldsymbol{V}}, \tilde{p})$ contains the most singular terms of the asymptotic expansion at both corners A and B. In the NS1 method, the singular part is defined as

$$\tilde{\boldsymbol{V}} = \boldsymbol{V}_1^A + \boldsymbol{V}_1^B, \qquad \tilde{p} = p_1^A + p_1^B \tag{49}$$

so that the following behaviour is found for the computed solution near $s = A$:

$$\bar{\boldsymbol{V}} + \boldsymbol{V}_1^B \sim Re\, r \boldsymbol{F}_2(\theta), \qquad \bar{p} + p_1^B \sim \log r G_2(\theta) \tag{50}$$

the fields $\boldsymbol{V}_1^B$ and p_1^B being smooth in the region. An analogous behaviour is found near corner B. Note that in the NS1 method, the computed pressure is unbounded near the upper corners. The NS2 method consists in subtracting not only the first (Stokes) term at $s = A$, B, but also the first Navier–Stokes term, according to

$$\tilde{\boldsymbol{V}} = \boldsymbol{V}_1^A + \boldsymbol{V}_2^A + \boldsymbol{V}_1^B + \boldsymbol{V}_2^B, \qquad \tilde{p} = p_1^A + p_2^A + p_1^B + p_2^B \tag{51}$$

The behaviour of the computed solution near $s = A$ is then

$$\bar{\boldsymbol{V}} + \boldsymbol{V}_1^B + \boldsymbol{V}_2^B \sim Re^2 r^2 \boldsymbol{F}_3(\theta), \qquad \bar{p} + p_1^B + p_2^B \sim Re\, r G_3(\theta) \tag{52}$$

At corners C and D, where no treatment is considered, the behaviour of $(\bar{\boldsymbol{V}}, \bar{p})$ for both subtraction methods is given by the first Stokes term

$$\bar{\boldsymbol{V}} + \tilde{\boldsymbol{V}} \sim K_{\lambda_1}(t) r^{2.74} [\cos(1.13 \log r) \mathbf{g}_v(\theta) + \sin(1.13 \log r) \mathbf{h}_v(\theta)] \tag{53a}$$

$$\bar{p} + \tilde{p} \sim K_{\lambda_1}(t) r^{1.74} [\cos(1.13 \log r) g_p(\theta) + \sin(1.13 \log r) h_p(\theta)] \tag{53b}$$

Thus, the solution computed by the subtraction method is more regular at these corners than at A and B. Note that the computed solution $(\bar{\boldsymbol{V}}, \bar{p})$ is submitted to the influence of the time discretization error. It is expected that the behaviour of the computed solution is not greatly affected by this error in so far as the third-order scheme is used for the calculation of unsteady flows.

Extensive numerical results on steady cavity flows, mainly for the flow at $Re = 1000$, obtained with the NS2 method, were previously reported by Botella and Peyret [22]. In the following, we mainly focus on evaluating the accuracy given by the subtraction technique. For that purpose, the NS0, NS1 and NS2 methods are applied to the calculation of the steady flow (defined by the criterion (43) with $\epsilon = 10^{-10}$) at $Re = 1000$. A first qualitative evaluation is made when comparing the isovorticity lines of the NS0 solution (i.e. no singular terms are subtracted, Figure 3(a)) and the NS2 solution (Figure 3(b)). Each figure displays the same contour lines obtained from a $N = N_x = N_y = 128$ truncation solution, interpolated on a fine 513×513 Gauss–Lobatto grid. The efficiency of the subtraction method is made clear by observing that the Gibbs oscillations displayed by the NS0 solution have disappeared when the NS2 method is employed. We mention that, at the scale of the figures, the isovorticity lines obtained with the NS1 method are indistinguishable from those displayed for the NS2 solution.

Figure 4(a) shows the spectrum $\{|\hat{\bar{\omega}}_k|,\ k = 0, \ldots, N\}$ of the expansion of the computed vorticity $\bar{\omega}$ in its Chebyshev basis along the boundary AD. Note that in the NS0 method $\bar{\omega} = \omega$ since no singular term is subtracted. For this method, where the vorticity behaves like $1/r$ near corner A, no decay of the spectral coefficients is observed. On the other hand, it can be clearly seen that the more the solution is smooth, the more the coefficients decay faster. Nevertheless, the decay is slow and does not exhibit an exponential rate since the computed solutions are weakly singular at corner A: the first derivative of the vorticity obtained from the NS1 solution and the second derivative of the vorticity obtained from the NS2 solution are unbounded. The spectrum of $\bar{\omega}$ along the midline $x = 1/2$ is displayed in Figure 4(b). On this line located at an equal distance far from the singular corners A and B, an exponential decay of the first coefficients of the Chebyshev expansion of the solution is observed. A saturation of the decay is nonetheless observed at the tail of the spectrum, testifying of a pollution effect due to the presence of the singularities.

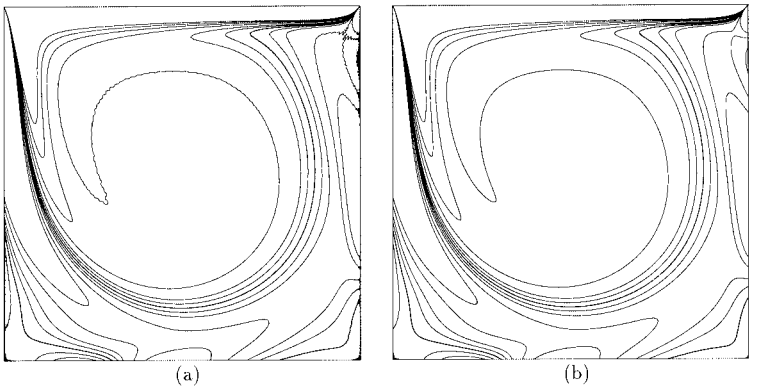

Figure 3. Isovorticity lines of the flow at $Re = 1000$, for $N = 128$. (a) NS0 solution and (b) NS2 solution.

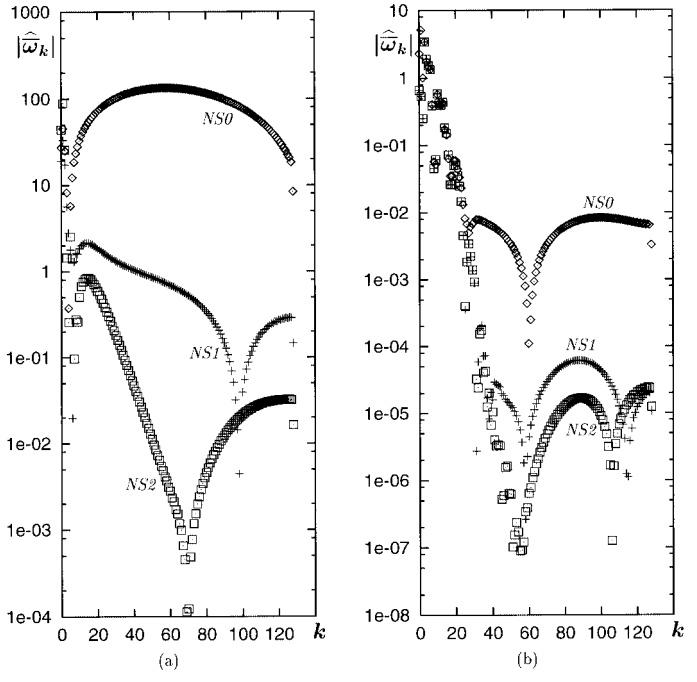

Figure 4. Chebyshev spectrum of $\bar{\omega}$ along (a) the boundary $x = 0$ and (b) the mid-line $x = 1/2$ obtained by the various methods for the flow at $Re = 1000$, with $N = 128$.

The global approximation rate of the subtraction method has been measured by estimating the continuous error norms $\|\boldsymbol{V}_N - \boldsymbol{V}_{\text{ref}}\|_{L^2_w(\Omega)}$ for the velocity and $\|p_N - p_{\text{ref}}\|_{L^2_w(\Omega)}$ for the pressure. The complete solution decomposes as

$$\boldsymbol{V}_N = \tilde{\boldsymbol{V}} + \bar{\boldsymbol{V}}_N, \qquad p_N = \tilde{p} + \bar{p}_N$$

where $(\bar{\boldsymbol{V}}_N, \bar{p}_N)$ is the solution computed on the $(N+1) \times (N+1)$ collocation grid. The field $(\boldsymbol{V}_{\text{ref}}, p_{\text{ref}}) = (\tilde{\boldsymbol{V}} + \bar{\boldsymbol{V}}_{\text{ref}}, \tilde{p} + \bar{p}_{\text{ref}})$ denotes a solution sufficiently accurate for the evaluation of the errors. This reference solution is chosen as the NS2 solution with $N = 160$, which has proved in Reference [22] to be our most accurate solution. The above norms are estimated by using quadrature formulae as described in Section 2.

Figure 5(a) and (b) displays, respectively, the L^2_ω error on the velocity and the pressure versus the degrees of freedom N measured for the various methods. The rate of the decay of the error that is reached asymptotically is compared in Table VI with the interpolation rate of the computed solution $(\bar{\boldsymbol{V}}, \bar{p})$, the latter being obtained by a direct application of formula (17) for functions displaying a singularity in $r^\alpha f(\theta)$ at a corner of Ω. We recall that the behaviour of the solution computed by the NS1 and NS2 methods is given by Equations (50) and (52)

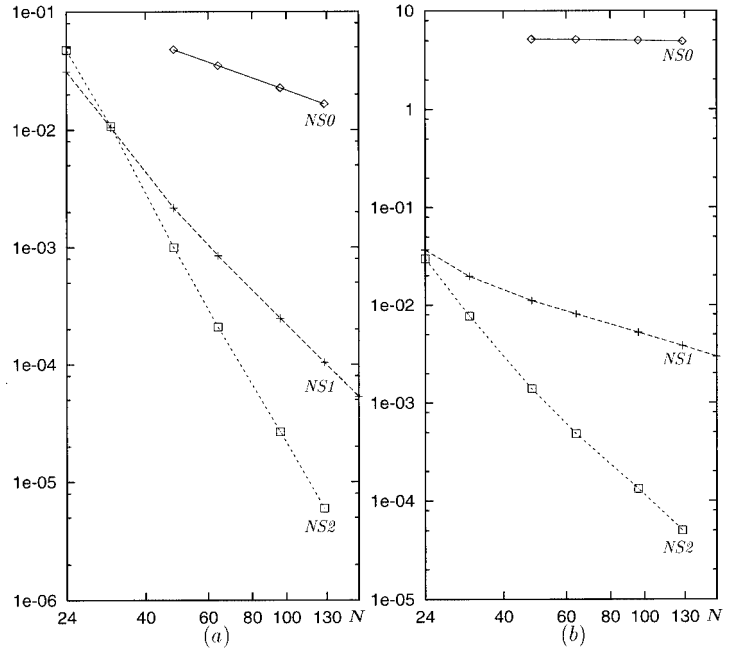

Figure 5. Global approximation error in the L^2_ω norm obtained by the various methods for (a) the velocity and (b) the pressure; lid-driven cavity flow at $Re = 1000$.

Table VI. Comparison of the global approximation rate and the interpolation rate of the solution computed by the various methods; flow in the lid-driven driven cavity at $Re = 1000$.

	NS0	NS1	NS2
$\|\boldsymbol{V}_N - \boldsymbol{V}_{\text{ref}}\|_{L^2_w(\Omega)}$	1.1	3.0	5.1
Interpolation of $\bar{\boldsymbol{V}}$, Equation (17)	1	3	5
$\|p_N - p_{\text{ref}}\|_{L^2_w(\Omega)}$	—	1.1	3.2–3.4
Interpolation of $\bar{p}$, Equation (17)	—	—	3

respectively. The results of Table VI show the good adequation of the approximation rate of the velocity with the one predicted by Equation (17). This illustrates the efficiency of the subtraction method and shows, in particular, that the overall numerical method gives an approximation rate for the velocity that is optimal since it matches the interpolation rate of the solution.

As for the velocity, the convergence rate of the computed pressure is in good agreement with the interpolation rule (17): while no accuracy can be obtained with the NS0 method, the

pressure computed with NS1, even if weakly singular (see Equation (50)), is first-order accurate. However, note that the convergence rate measured for the NS2 method is slightly superior to the one predicted by Equation (17). This rate is somewhat optimistic since $\bar{p}_{\text{ref}}$ may not be accurate enough for properly evaluating the NS2 errors, mainly for $N = 128$. The results of Table VI would suggest that the Inf–Sup constant (see, e.g. References [23,26]) of the projection step (42) is independent of N, so that the approximation of the pressure by our spectral scheme is optimal. We are not aware of theoretical results on the literature about this property.

The accuracy of the subtraction method has also been checked for the Stokes flow (see Reference [22] for further numerical results). Since the non-linear singularities $r^2 f_2^s$ and $r^3 f_3^s$ in Equation (48) are irrelevant, the subtraction of the first singularity $r f_1^s$ at $s = A, B$ (i.e. NS1 method) yields a computed solution whose regularity is analogous to Equation (53) at each corner of Ω. For that flow, it has been measured that the L^2_ω error on the velocity and the pressure behave asymptotically like $100N^{-6.5}$ and $50N^{-4.2}$ respectively. As for the non-linear case, these approximation errors are in good agreement with estimation (17), even though this last formula does not take into account the trigonometric and logarithmic terms involved in Equation (53).

The above convergence rates concern the accuracy of the method in a global sense only. The pollution effect of the singularities extends along the boundaries and it has been observed in References [22,28] that the largest errors are localized in these zones. In the largest part of the domain, the solution is not greatly affected by the singularities, and the pointwise accuracy is much better than the one evaluated in the L^2_ω norm. As an example, the pointwise accuracy obtained on the maximum of u on the line $y = 1/2$ is evaluated in $O(N^{-5})$ for the NS0 solution, and is, respectively, $O(N^{-9})$ and $O(N^{-17})$ for the NS1 and NS2 solution. In contrast, the accuracy of the solution, particularly the vorticity field, is weaker near the upper singular corners A and B; a filtering post-process has been employed in Reference [22] in order to improve the convergence of the pressure fields near these singular points.

A further illustration of the accuracy and the efficiency of the subtraction method is given by computation of the unsteady flow that appears after a first Hopf bifurcation occurring at a critical Reynolds number Re_c. In Reference [39], the study of the eigenvalues of the discretized system has detected this bifurcation at $Re_c \simeq 7763$. The flow at $Re = 9000$ is computed with the NS1 and NS2 methods by means of the third-order scheme described in Section 4. The spatial resolution is defined by $N = 96$, which is rather coarse for this value of Re, and the time step is $\Delta t = 8 \times 10^{-4}$. The criterion used for monitoring the time evolution of the flow is the discrete kinetic energy $E_c(t)$, defined by

$$E_c(t) = \left\{ \sum_{i,j=0}^{N} u^n(x_i, y_j)^2 + v^n(x_i, y_j)^2 \right\}^{1/2}, \quad \text{with } u^n = \bar{u}^n + \tilde{u}, \quad v^n = \bar{v}^n + \tilde{v} \tag{54}$$

The periodic state is considered to be reached when the difference of two consecutive extrema of $E_c(t)$ is below 10^{-9}. The steady flow at $Re = 1000$ is taken as an initial condition for the NS1 computation and the periodic state is obtained after more than two million time cycles. The NS2 solution is obtained by starting the computation with the time periodic NS1 solution. Figure 6(a) and (b) displays the isobaric lines of the NS2 solution respectively at times

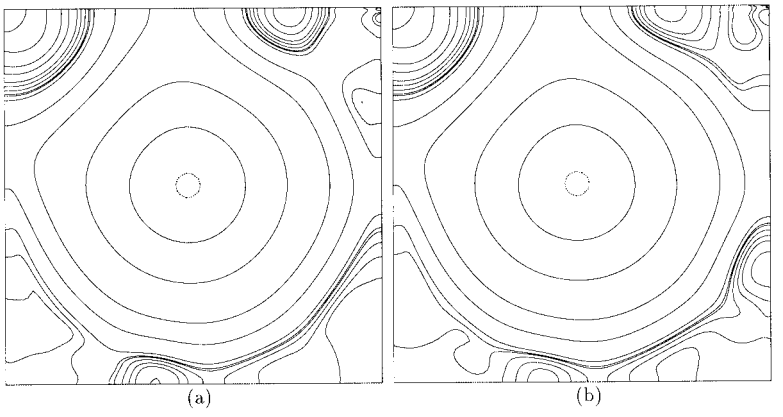

Figure 6. Isobaric lines of the periodic flow at $Re = 9000$ computed by the NS2 solution at the time (a) $t = 664.7688$ and (b) $t = 665.8152$.

corresponding to the minimum and maximum of the kinetic energy. Note that these lines display no oscillations, even though the spatial discretization is coarse.

Some characteristic results of the periodic solution are given in Table VII. In this table, the maximal and minimal values of the kinetic energy during one period are denoted $Ec_{\max}$ and $Ec_{\min}$ respectively. In the same fashion ($u_{\max}$, $u_{\min}$) and ($v_{\max}$, $v_{\min}$) refer to the extreme of u and v at the location (0.5, 0.5) during one period. Note that both solutions are close: the difference between the period T of the extrema of the kinetic energy computed by the NS1 and NS2 methods is only Δt.

The numerical results presented in this section show the dramatic enhancement of the approximation rate when the subtraction method is used. The computation of the periodic flow proves that this technique can be employed to compute unsteady singular flows at high Reynolds numbers, as long as the boundary conditions are non-homogeneous and the asymptotic expansion completely determined. As it will be shown in the next section, a refinement of the subtraction method has to be made for a non-homogeneous problem whose asymptotic solution admits the addition of an arbitrary eigensolution, so that a constant has to be determined from the consideration of the global solution.

Table VII. Characteristic results on the periodic flow in the lid-driven cavity at $Re = 9000$.

	T	$Ec_{\max}$	$Ec_{\min}$	$u_{\max}$	$u_{\min}$	$v_{\max}$	$v_{\min}$
NS1	$2.2464 \pm 8 \times 10^{-4}$	0.33401	0.33372	0.02748	0.02707	0.00943	0.00902
NS2	$2.2456 \pm 8 \times 10^{-4}$	0.33414	0.33386	0.02752	0.02711	0.00942	0.00901

6. INJECTION OF A FLUID INTO A CHANNEL

This application deals with the injection of a viscous fluid into a channel with a constant velocity profile. The fluid motion is governed by the Navier–Stokes equations, to be solved in the domain $\Omega =]0, 4[\times]0, 1[$. The boundary conditions associated with this problem are

$$\left.\begin{array}{ll} \boldsymbol{V} = (1, 0) & \text{if } \dfrac{1}{3} \le y \le \dfrac{2}{3} \\ \boldsymbol{V} = \boldsymbol{0} & \text{otherwise} \end{array}\right\} \quad \text{at the upstream boundary } x = 0$$

a parabolic profile for the velocity $\boldsymbol{V} = (2y(1-y), 0)$ at the downstream boundary $x = 4$, and $\boldsymbol{V} = \boldsymbol{0}$ on the other two sides. The Reynolds number is defined by taking as reference parameters the width of the channel and the velocity of the fluid at the upstream boundary.

The discontinuity of the velocity profile at the upstream boundary induces singularities that, contrary to the driven cavity problem, are no longer located at the corners. As suggested by the interpolation rates (16) and (17), the effects of the singularities on the numerical solution of the injection problem are much greater than for applications with corner singularities. More precisely, the asymptotic analysis shows that at the singular points $A(0, 1/3)$ and $B(0, 2/3)$, the vorticity and pressure are infinite and behave like $1/r$.

For the purpose of determining the first terms of the asymptotic solution near the points A and B, it is convenient to consider the model problem sketched in Figure 7, where the Navier–Stokes equation (18) is to be solved in the half plane $\{(r, \theta), 0 \le \theta \le \pi\}$, with the boundary conditions

$$\frac{\partial \psi}{\partial r} = -1, \quad \frac{\partial \psi}{\partial \theta} = 0 \quad \text{on the side } \theta = 0, \qquad \frac{\partial \psi}{\partial r} = 0, \quad \frac{\partial \psi}{\partial \theta} = 0 \quad \text{on the side } \theta = \pi \tag{55}$$

The determination of the first terms of the Navier–Stokes equations is performed in a fashion similar to the one described in Section 3. We anticipate the following by mentioning that it will be found necessary to introduce logarithmic terms in the expression of the singular solution, and that the first Navier–Stokes term cannot be determined completely by the local analysis. It will be shown that this term involves a constant that depends on the global flow. This constant will be determined numerically by using an iterative process.

The solution near the point s is sought of the form (20) satisfying Equation (23). The first term $\psi_1 = r^{\alpha_1} f_1(\theta)$ is such that f_1 satisfies $L_{\alpha_1} f_1 = 0$ with $\alpha_1 = 1$ (from the boundary conditions (55)). The expression of f_1 is found to be

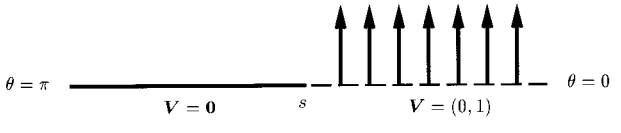

Figure 7. Model singular problem for the injection application.

$$f_1(\theta) = \frac{1}{\pi}\left[(\theta - \pi)\cos\theta - \sin\theta\right] \tag{56}$$

As for the model problem described in Section 3, the Stokes system admits eigenfunctions of the form $\psi_\lambda = r^\lambda f$, where λ is the solution (else than 1, which gives $f_1 = 0$) of Equation (22) with $\theta = \pi$, namely λ is any positive integer greater than 1. Therefore, the lowest eigenvalue is $\lambda_1 = 2$, and the associated expression of ψ_{λ_1} is

$$\psi_{\lambda_1} = r^2 K_{\lambda_1}(\cos 2\theta - 1) \tag{57}$$

where K_{λ_1} is an arbitrary constant.

The determination of the second term (first Navier–Stokes term) ψ_2 leads to some trouble. More precisely, the cancellation of the corresponding terms in Equation (23) gives $\alpha_2 = 2$, and f_2 is solution to the non-homogeneous equation (30) with homogeneous boundary conditions deduced from Equation (55). In fact, the obtained differential problem is not solvable because it leads to a non-homogeneous linear system for the coefficients of f_2, which has no solution since its determinant is zero with a non-compatible right-hand side. The reason is that $\alpha_2 = 2$ is both an eigenvalue of the Stokes problem and the exponent of the first Navier–Stokes term of the asymptotic expansion. Therefore, the form (20) of this expansion is not suitable for that problem. As it is often the case for this type of asymptotic expansion (see, e.g. Reference [40,41]), it is found necessary to introduce logarithmic terms into expansion (20), namely the term ψ_2 is now considered as

$$\psi_2 = r^2 \log r \;\; g_2(\theta) + r^2 f_2(\theta) \tag{58}$$

Thus, the simultaneous cancellation of the terms in $r^2 \log r$ and r^2 of Equation (23) leads to the differential equations

$$\mathscr{L}_2 g_2 = 0 \tag{59a}$$

$$\mathscr{L}_2 f_2 + 4g_2'' = Re\,\mathscr{N}_{1,1}(f_1, f_1) \tag{59b}$$

with appropriate homogeneous boundary conditions obtained from Equation (55) for both g_2 and f_2. Note that Equation (59a) determines g_2 up to an arbitrary constant c_2. Furthermore, the determination of f_2 by Equation (59b) leads to a linear system whose determinant is zero, as before. However, it is now possible to choose c_2 such that its right-hand side is made compatible. As a result, the function f_2 can be calculated and thus the first Navier–Stokes term ψ_2 reads

$$\psi_2 = \frac{r^2 Re}{32\pi^2}\left[(\cos 2\theta - 1)(2\pi \log r + 8K_2 - 7\theta) + 2(\pi - \theta)\theta \sin 2\theta\right] \tag{60}$$

but the constant K_2 is unknown. It can be observed that the K_2 term in Equation (60) is nothing but the eigenfunction (57). This testifies that it is possible to add such an eigenfunction

to the solution ψ_2. The part in $r^2 \log r$, which is the leading part of ψ_2, is completely determined. Moreover, it can be observed that the undetermined part is smooth since it is a quadratic monomial in Cartesian co-ordinates. Thus, discarding this part (by posing $K_2 = 0$) does not reduce the regularity of the solution computed by the NS2 subtraction method. As a matter of fact, this regularity is governed by the third term of the asymptotic solution

$$\psi_3 = r^3 \log^2 r \;\; h_3(\theta) + r^3 \log r \;\; g_3(\theta) + r^3 f_3(\theta) \tag{61}$$

obtained in a fashion similar to the one described for ψ_2. The functions h_3 and g_3 are completely determined but not f_3, since $\alpha_3 = 3$ is an eigenvalue of the Stokes problem. Note also that ψ_3 is proportional to Re^2.

It has to be mentioned that the expression of ψ_2 can also be obtained by a technique due to Moffatt and Duffy [40] (see also Reference [11]). This technique amounts to building the asymptotic expansion in the case where the boundaries intersect with the angle $\theta = \pi - \epsilon$, with $\epsilon > 0$. The first Navier–Stokes term $\psi_{2,\epsilon}$ is completely determined in this configuration, since the lowest eingenvalue $\lambda_{1,\epsilon}$ is different from 2. In the limiting case $\epsilon \to 0$, both the eigenfunction $\psi_{\lambda_{1,\epsilon}}$ and $\psi_{2,\epsilon}$ observe a singular behaviour in $1/\epsilon$ that can be eliminated by choosing the arbitrary constant in $\psi_{\lambda_{1,\epsilon}}$ such that $\psi_{2,0} = \lim_{\epsilon \to 0} [\psi_{\lambda_{1,\epsilon}} + \psi_{2,\epsilon}]$ is finite. As a result, the expression of $\psi_{2,0}$ to the one given in Equation (60), with the exception that the constant K_2 is identified and is equal to $7\pi/8$. Nevertheless, we point out that it is still possible to add eigenfunction (57) to $\psi_{2,0}$ such that only the part in $r^2 \log r$ is completely determined.

As an illustration, the steady flow at $Re = 100$ is computed by treating the singularities at $A(0, 1/3)$ and $B(0, 2/3)$ by using the subtraction method. The singular part of the NS1 solution is completely determined by the above asymptotic analysis. On the other hand, the singular part of the NS2 solution is determined up to the constant K_2 (by using the symmetry of the problem, it is easily shown that the undetermined constants K_2^s for $s = A, B$ verify $K_2^A = K_2^B = K_2$). As stated previously, the use of the NS2 method with an arbitrary value of K_2 only subtracts the (main) singularity in $r^2 \log r$, and does not affect the regularity of the computed solution. It is nonetheless interesting to compute this constant which, for example, would be necessary to calculate the higher-order term of the asymptotic expansion. The problem of its determination is also related to the treatment of singular solutions in the case of homogenenous boundary conditions and, in these respects, is of interest. A typical example of such problems in fluid mechanics is given by the flow in a channel with a sudden expansion (see, e.g. [5,14,16]). The constants involved in the expansion of the solution near the singular corner need to be determined as a part of the numerical solution. In the first two references, they are determined by an iterative matching of the dominant part of the asymptotic solution with a numerical solution computed outside a small neighbourhood of the corner. The third reference uses the singular finite element method, where the behaviour of the first terms of the expansion is incorporated in the trial function basis. It should be noted that the leading part of the expansion represents only the solution at a distance from the corner that decreases inversely with the Reynolds number. So, any of these methods needs grid points sufficiently near the corner to obtain a satisfactory accuracy, and their clustering must be chosen according to the value of the Reynolds number.

The technique used here for the determination of K_2 bears some similarity to both methods. As in Reference [14], the fields $(\bar{V}, \bar{p})$ are computed in the whole domain from the set of Equations (37) and (39), where the form of the singular solution is incorporated. As in References [5,16], the constant K_2 is then iteratively determined by imposing that in the vicinity of a singular point (say $s = A$), the complete solution (V, p) is accurately represented by the first two singular terms. According to the construction of the asymptotic solution, this approximation is only valid within a distance r to A, where the contribution of the following terms is negligible, i.e. we get from Equations (60) and (61)

$$r \log^2 r \ll Re^{-1} = 10^{-2} \tag{62}$$

As a result, this would imply that $(\bar{V}, \bar{p})$ behaves like the third term in the asymptotic expansion, i.e. the value of K_2 is determined so that the second term is completely subtracted. Note that since the flow is symmetric, an analogous behaviour is observed near $s = B$.

In practice, this iterative process is assimilated here to the time integration since the calculated flow is steady and K_2 does not depend on time. The initial condition is defined as the rest, where the initial guess of K_2 is $K_2^0 = 0$. At $t = n\Delta t$, the fields (V^n, p^n) are computed by means of the projection scheme with the value K_2^{n-1} obtained at the previous time level; the value K_2^n is then calculated by requiring that at the point P, located at a distance r_p from A such that Equation (62) is verified

$$V^n(P;\ K_2^{n-1}) = V_1^A(P) + V_2^A(P;\ K_2^n) \tag{63}$$

where V_1^A and V_2^A refer to the first two terms of the asymptotic solution near A. From Equation (60), the part V_2^A is of the form

$$V_2^A(P;\ K_2) = V_{2,1}^A(P) + K_2 V_{2,2}^A(P)$$

so that K_2^n in Equation (63) can be explicitly evaluated. This algorithm is considered to reach convergence when $|K_2^n - K_2^{n-1}| < 10^{-9}$ and the steady state criterion (43) with $\epsilon = 10^{-9}$ is fulfilled. We point out that in this algorithm, the matching between the asymptotic and computed solution is performed at a single point only. A refinement of this technique would be to consider a least-squares matching, as in Reference [5,16]. Expression (62) clearly shows that for a given computational grid, the accuracy obtained on K_2 depends essentially on the nearness of P to A. As a result, the use of a grid point as the location of P would require to cluster the mesh in the vicinity of A so that Equation (62) is valid. In contrast, by using the properties of the Chebyshev polynomial approximation it is possible to evaluate expression (63) at a point P sufficiently near A in order to obtain K_2 with a high accuracy. Table VIII summarizes the values of K_2 for the flow at $Re = 100$, obtained when various locations of P are used in the iterative algorithm with a grid defined by $N_x = 96$ and $N_y = 128$. In the first computation (second line of Table VIII), point P is chosen as the inner collocation point that is the closest to A. Nevertheless, expression (63) seems not to be valid at this location of P, so

Table VIII. Values of K_2 obtained for the flow at $Re = 100$ when the iterative algorithm is used with various locations for P.

Point P	$r_p \log^2 r_p$	K_2
Collocation point, $r_p \simeq 2 \times 10^{-3}$	8×10^{-3}	3.8174325
$(r_p, \theta_p) = (10^{-8}, 0)$	3×10^{-6}	3.8121106
$(r_p, \theta_p) = (10^{-8}, \pi/4)$	3×10^{-6}	3.8121105

The co-ordinates of P are given in the polar system of origin A, defined by $x_p = r_p \cos \theta_p$, $y_p = 1/3 + r_p \sin \theta_p$.

that the first two terms of the asymptotic solution might not be dominant. Further computations were performed by taking P much nearer of A, at a location that is no more a collocation point. In this fashion, it is possible to obtain K_2 with an 8-digit accuracy as shown in Table VIII. These results illustrate the fact that the evaluation of K_2 needs to be performed as close as possible to A.

The isovorticity lines given by the NS0 and NS2 methods are compared in Figure 8. Note that at the scale of this figure, the isolines obtained with the NS1 method are indistinguishable from those displayed by the NS2 solution. It is worthwhile to recall that the vorticity is infinite at points A and B. Thus, these points are not used for the plots shown in this figure and one that follows. It can be observed from Figure 8(a) that huge oscillations are apparent in the NS0 solution near the upstream boundary. Nevertheless, when compared with the lines given by the NS2 method, these oscillations seem to affect only the flow on the first vertical lines of the grid. Figure 9 displays the corresponding vorticity profiles at the upstream boundary. The

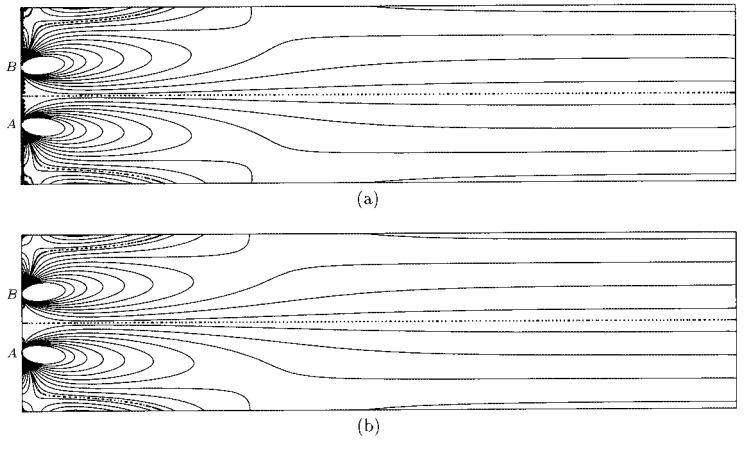

Figure 8. Isovorticity lines of the flow at $Re = 100$, with $N_x = 96$ and $N_y = 128$, (a) NS0 solution, (b) NS2 solution.

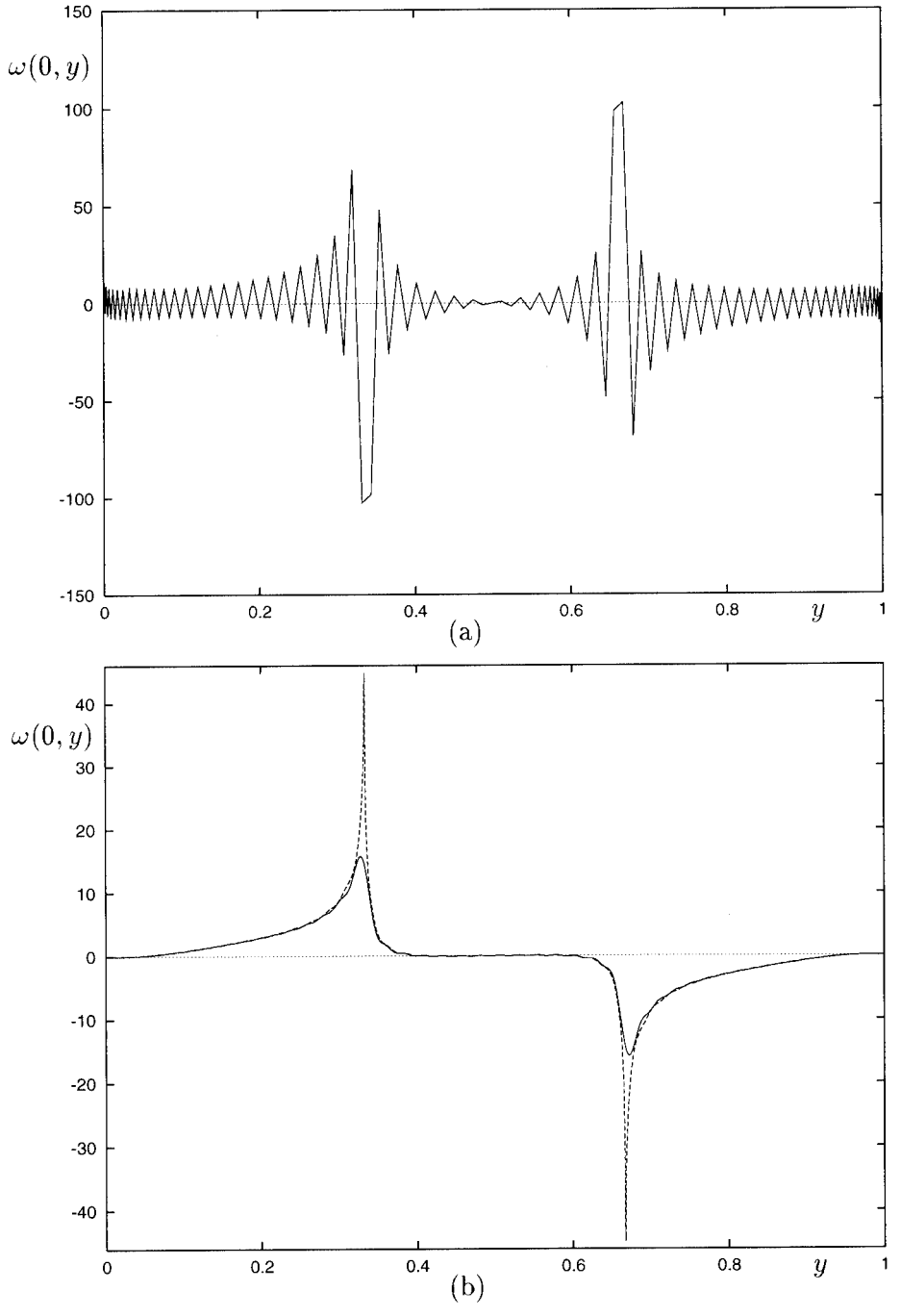

Figure 9. Vorticity profile on the upstream boundary for the flow at $Re = 100$. (a) NS0 solution at the collocation points, (b) NS1 solution (solid line) and NS2 solution (dashed line) interpolated on 1001 equidistant points.

NS0 profile (Figure 9(a)) is entirely polluted by Gibbs oscillations. Owing to the global nature of the spectral approximation, the singular behaviour in $1/r$ of the vorticity induces oscillations that spread along the whole boundary. These oscillations have almost disappeared from the NS1 and NS2 profiles (Figure 9(b)). The difference in the profiles displayed in this last figure near the singular points is due to the fact that the singular vorticity term ω_2^s (corresponding to the term ψ_2^s), which grows like $\log r$ near $s = A, B$, is part of the solution computed by NS1, while this term is contained in the analytical part of the NS2 solution. This also means that the vorticity computed by NS1 is still unbounded while it behaves like $r \log^2 r$ for the NS2 method.

Finally, it must be noticed that the effect of the singularities on the accuracy of the computations is not only localized near the upstream boundary. Figure 10 displays the profile of the u component of the velocity along the section $x = 2$. At this distance from the upstream boundary, the NS2 solution is very accurate: the profiles obtained with a grid of 97×65 points and 97×129 points are indistinguishable at the scale of the figure. In contrast, the NS0 solution computed with the same grids has clearly not yet spatially converged. This shows that when the singularities in $s = A, B$ are not treated, a numerical pollution phenomenon degrades the accuracy of the solution away from the upstream boundary. This pollution phenomenon is much more severe here than in the driven cavity application, where the accuracy of the NS0 solution proved to be satisfactory in the centre of the domain.

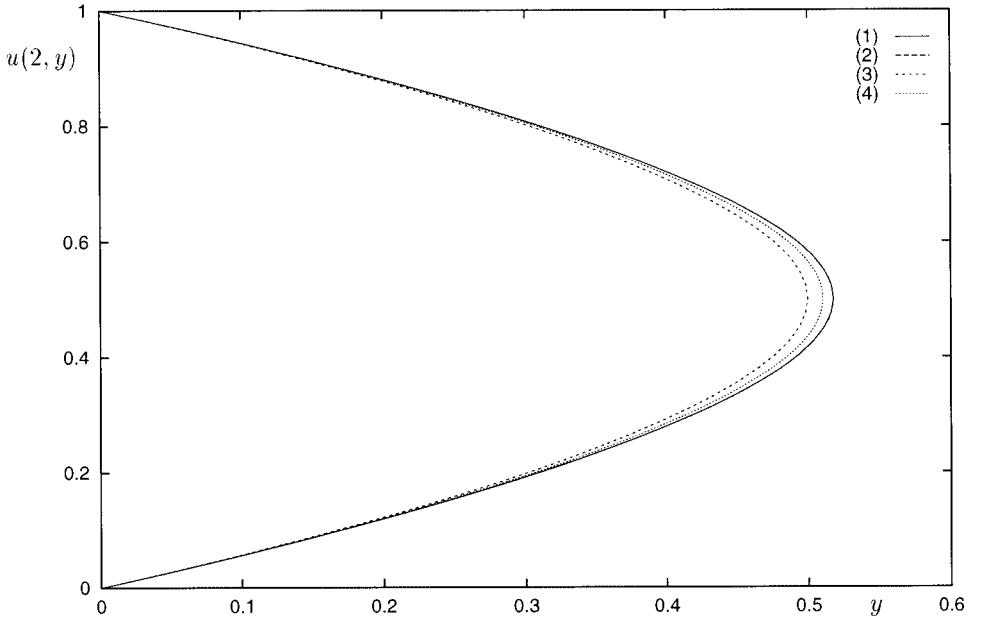

Figure 10. Profile of the velocity u in the section $x = 2$ for the flow at $Re = 100$, given by the NS2 method with (1) the 97×65 grid, (2) the 97×129 grid, and by the NS0 method with (3) the 97×65 grid, (4) the 97×129 grid. Note that the curves labelled (1) and (2) coincide at the scale of the figure.

7. FLOW IN A TWO-DIMENSIONAL PISTON ENGINE

Finally, the subtraction method is applied to the unsteady flow in a two-dimensional piston engine. The Navier–Stokes equations for a compressible fluid are simplified by using the assumptions usually made for this type of flow [42–44], i.e. the Mach number is low, and that the fluid density ρ is homogeneous in space and is a function of time alone. As a result, by using the ideal gas law, the temperature T depends only on time and the energy equation plays no role. Furthermore, the system can be put into a simpler form by decomposing the variables into a basic flow, taking into account the compressibility effect, and an incompressible perturbation flow $V' = (u', v')$ and p' such as

$$\boldsymbol{V} = \hat{\boldsymbol{V}} + \boldsymbol{V}', \qquad p = \hat{p} + p', \qquad \rho = \hat{\rho}, \qquad T = \hat{T} \tag{64}$$

as done by Pascal and Buffat [44] for the turbulent flow compressed between two parallel planes. The above quantities are dimensionless. The reference velocity is chosen as the maximal speed of the piston. The reference quantities for pressure and density are their values at the initial time. The reference length is the maximal height of the piston, so that at $t = 0$ the computational domain is $\Omega_0 = \{0 < X < 1, 0 < Y < 1\}$. At $t > 0$, the domain $\Omega_t = \{0 < X < 1, 0 < Y < Y_p\}$ is compressed in the Y-direction such as $Y_p = L(t)$, with $L(0) = 1$, is the dimensionless instantaneous piston height (see Figure 11). The boundary conditions are $\boldsymbol{V} = (0, \dot{L}(t))$ on $Y = Y_p$ and $\boldsymbol{V} = 0$ on the other three sides. The initial condition $\boldsymbol{V}^0$ will be defined later. Note that when the piston is moving, these boundary conditions display discontinuities at the contact points $\mathscr{A}(0, Y_p)$ and $\mathscr{B}(1, Y_p)$, where the piston meets the walls of the engine. After transforming the physical domain Ω_t into the fixed domain $\Omega = \{0 < x < 1, 0 < y < 1\}$ by the co-ordinate mapping $x = X$, $y = Y/L(t)$, and performing a change of dependent variables, the non-dimensional equations for the transformed perturbations ($\boldsymbol{v} = (u, v)$, π) are

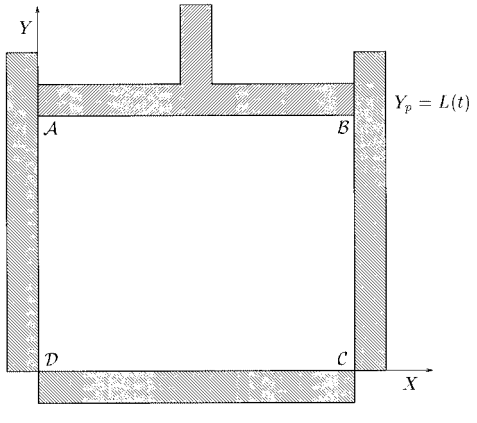

Figure 11. Sketch of the two-dimensional piston engine.

$$\frac{\partial u}{\partial t}+u\frac{\partial u}{\partial x}+\lambda v\frac{\partial u}{\partial y}-\frac{v}{Re}\left(\frac{\partial^2 u}{\partial x^2}+\lambda\frac{\partial^2 u}{\partial y^2}\right)+\frac{1}{\hat{\rho}}\frac{\partial \pi}{\partial x}=0 \tag{65a}$$

$$\frac{\partial v}{\partial t}+u\frac{\partial v}{\partial x}+\lambda v\frac{\partial v}{\partial y}-\frac{v}{Re}\left(\frac{\partial^2 v}{\partial x^2}+\lambda\frac{\partial^2 v}{\partial y^2}\right)+\frac{1}{\hat{\rho}}\frac{\partial \pi}{\partial y}=0 \tag{65b}$$

$$\frac{\partial u}{\partial x}+\lambda\frac{\partial v}{\partial y}=0 \tag{65c}$$

where $u=u'$, $v=L(t)v'$ and $\pi=p'$. These equations have a form similar to the Navier–Stokes equations for an incompressible fluid, with the difference that the quantities $\lambda=1/L^2(t)$ and $\hat{\rho}=L(0)/L(t)$ appear in the operators. The dimensionless kinematic viscosity is supposed to follow the law $v=\hat{T}^{3/4}/\hat{\rho}$ discussed in Reference [45], so that

$$v=\hat{\rho}^{(3\gamma-7)/4}, \quad \text{with } \gamma=1.4 \tag{66}$$

i.e. v is a function of the time that decreases as the domain is being compressed. The boundary conditions for the velocity perturbations are

$$u=0,\ v=0 \text{ on the sides } y=0 \text{ and } y=1 \tag{67a}$$

$$u=0,\ v=\beta y \text{ on the sides } x=0 \text{ and } x=1 \tag{67b}$$

with $\beta=-\dot{L}(t)L(t)$. When the piston is moving, these boundary conditions introduce singularities at the corners A, B, C and D of the computational domain, the latter being the respective images of $\mathscr{A}$, $\mathscr{B}$, $\mathscr{C}$ and $\mathscr{D}$ through the co-ordinate transform. At corners $A(0,1)$ and $B(1,1)$, the singularities are similar to those generated by the discontinuous boundary conditions in the driven cavity problem; the vorticity and the pressure are unbounded and behave like r^{-1}. The singularities at the corners $C(1,0)$ and $D(0,0)$, which are generated by the decomposition (64) of the dependent variables, are weaker since only the velocity derivatives are discontinuous. As a result, the vorticity gradient and the pressure behave like r^{-1} and $\log r$ respectively near these points.

After having defined the streamfunction by $u=\lambda\,\partial\psi/\partial y$, $v=-\partial\psi/\partial x$, the determination of the leading part of the asymptotic expansion near each singular point is a straightforward application of the technique described in Section 3. As $s=A$, B, the first terms of the singular solution reads

$$\psi=rf_1^s(\theta,t)+r^2f_2^s(\theta,t)+r^3f_3^s(\theta,t) \tag{68}$$

In particular, $\psi_1^s=rf_1^s$ is a Stokes term and $\psi_2^s=r^2f_2^s$ is a term generated by the inertia forces; both terms are unsteady due to boundary conditions (67). Note that, as stated previously in Section 3, time appears only as a parameter in these two terms, the first term generated by the unsteadiness being $\psi_3^s=r^3f_3^s$. The leading part of the singular expansion at $s=C$, D is found to be given by the following first two Stokes terms:

$$\psi = r^2 g_1^s(\theta, t) + r^{\lambda_1} g_2^s(\theta, t), \quad \text{with } \lambda_1 \simeq 3.74 + 1.12\underline{i} \tag{69}$$

where the second of this term is an eigenfunction that is only determined up to a multiplicative constant. Unless specified, the computations reported hereafter are obtained with a subtraction method where the first two terms of the expansion at $s = A, B$ and the first term at $s = C, D$ are subtracted. As a result, the regularity of the computed solution is the same as the one computed by the NS2 method for the driven cavity flow, i.e. it is reasonable to expect a $O(N^{-5})$ accuracy for the velocity and a $O(N^{-3})$ accuracy for the pressure. By analogy, this method is referred in the following as the NS2 method.

Numerical experiments of a compression stroke are performed by using various initial conditions defined by the Taylor–Green vortices

$$\boldsymbol{V}^0 = (\sin(m\pi x)\cos(m\pi y), \ -\cos(m\pi x)\sin(m\pi y)) \tag{70}$$

where the value of m will be defined later. The non-dimensional piston law is defined as

$$L(t) = \frac{1}{2}(1+\eta) + \frac{1}{2}(1-\eta)\cos\left(\frac{2t}{1-\eta}\right)$$

where $1/\eta$ is the total compression ratio, such as during the integration time $[0, t_c = (1-\eta)\pi/2]$, which corresponds to a compression stroke, the piston compresses the domain from $Y_p = 1$ at $t = 0$ to $Y_p = \eta$ at $t = t_c$. Note that $L(0) = L(t_c) = 0$, so that no spatial singularities are present at the beginning and at the end of the compression. The computations are performed by using the third-order scheme described in Section 4; the compatible pressure field needed for the starting scheme (Equations (44)–(46)) is

$$p^0 = (\cos(2m\pi x) + \cos(2m\pi y))/4$$

Let us evaluate the quality of the singularity treatment by comparing the spectra of the Chebyshev expansion of the solution obtained with the NS2 and NS1 method, the latter being defined by the subtraction of the first term of the asymptotic expansion at each corner. The parameters of the compression are $m = 1$ (i.e. a unique Taylor–Green vortex), $Re = 500$ and $\eta = 5 \times 10^{-2}$; the collocation grid is defined by $N_x = 256$ and $N_y = 128$ and the time step is $\Delta t = 4 \times 10^{-4}$. Figure 12 displays the spectra ($|\hat{\bar{u}}_k|$) of the first component $\bar{u}$ of the velocity computed by both methods on the first horizontal grid line under the $y = 1$ (i.e. corresponding to the piston boundary in the physical domain) at $t = 1.2726$ ($Y_p \simeq 0.1$) when the singularities are present. In this region, very close to the singular corners A and B, the benefit of subtracting the first two terms (NS2 method, $\bar{\boldsymbol{v}} \sim r^2$ at $s = A, B$) over the subtraction of the first term (NS1 method, $\bar{\boldsymbol{v}} \sim r$ at $s = A, B$) is clearly seen on the better decay of the Chebyshev coefficients.

Finally, we present results on a compression stroke taking as initial condition (70) with $m = 3$. This initial condition generates nine counter rotating vortices of equal intensity, whose streamlines are displayed in Figure 13(a). The parameters of the compression are $\eta = 0.1$, i.e.

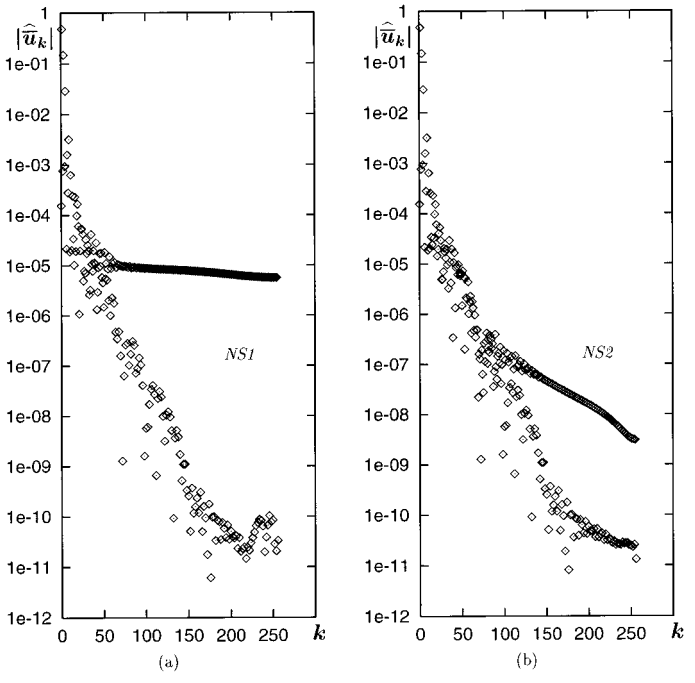

Figure 12. Chebyshev spectrum of $\bar{u}$ on the first horizontal line of the grid under the side $y = 1$, obtained by (a) the NS1 solution and (b) the NS2 solution (see the text for the parameters of the computation).

a total compression ratio of 10, the Reynolds number is $Re = 1000$, so that during the compression stroke the ratio Re/v increases from 1000 at $t = 0$ up to $10^{3.7} \simeq 5012$ at the end of the compression. The computational grid is defined by $N_x = 512$ and $N_y = 256$. The instantaneous streamlines of the flow are displayed in Figure 13 at various times of the compression stroke. At the beginning of the compression, the confinement effect is not strong enough to sustain the intensities of the initial vortices (Figure 13(a) and (b)). The final stage of the compression is characterized by the apparition of numerous small eddies, until a large number of eddies, with scales of the order of the piston height, fills the domain at the end of the compression (Figure 13(c)–(e)). This alignment of small vortices is qualitatively similar to the one observed by Naitoh *et al.* [42] in an axisymmetric piston engine. Figure 14 displays the isovorticity lines at the last stages of the compression. Let us mention that the vorticity does not display spurious oscillations during the compression process, attesting the efficiency of the subtraction method. The final stage of the compression shows the creation of large vortex sheets, characterizing the presence of strong gradients in the solution. It is indeed worthwhile observing that, in this problem, the computational difficulties are no more related to the treatment of corner singularities, but rather to the complex nature of the flow whose representation needs a high spatial resolution.

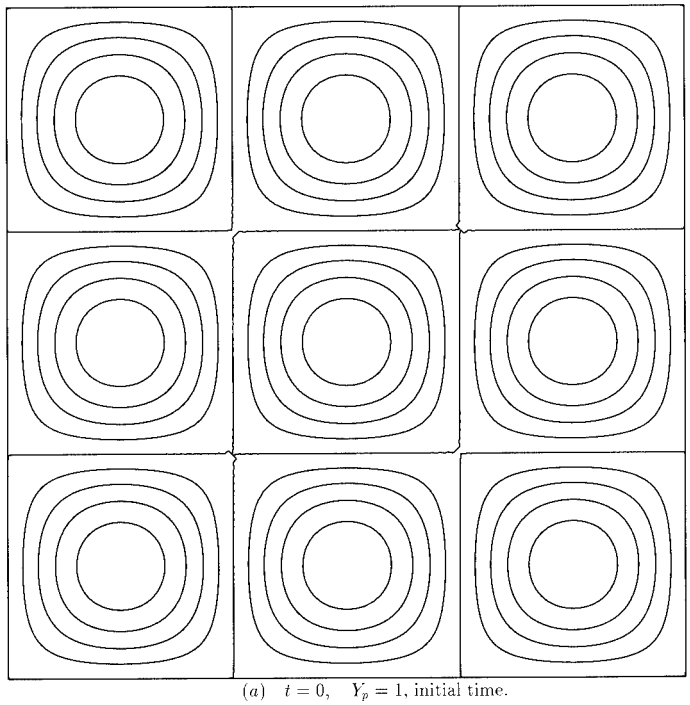

(a) $t = 0$, $Y_p = 1$, initial time.

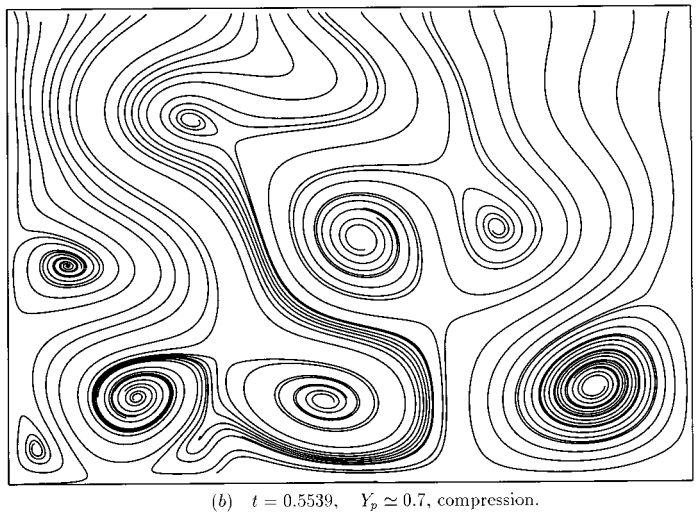

(b) $t = 0.5539$, $Y_p \simeq 0.7$, compression.

Figure 13. Instantaneous streamlines of the compression of nine Taylor–Green vortices. The domain is being compressed from top to bottom.

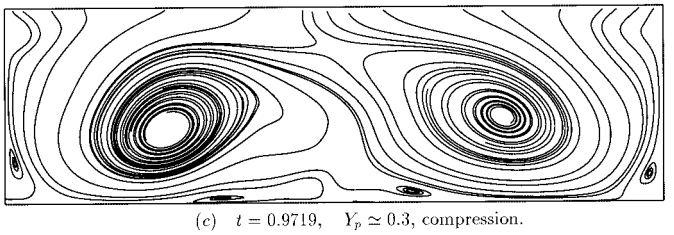

(c) $t = 0.9719$, $Y_p \simeq 0.3$, compression.

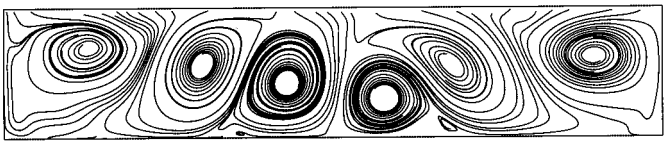

(d) $t = 1.10785$, $Y_p \simeq 0.2$, compression.

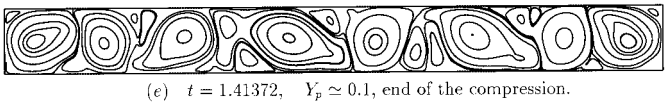

(e) $t = 1.41372$, $Y_p \simeq 0.1$, end of the compression.

Figure 13 (*Continued*)

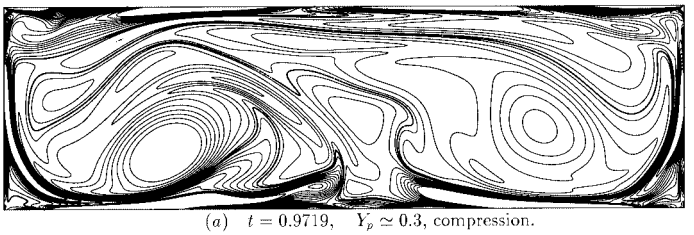

(a) $t = 0.9719$, $Y_p \simeq 0.3$, compression.

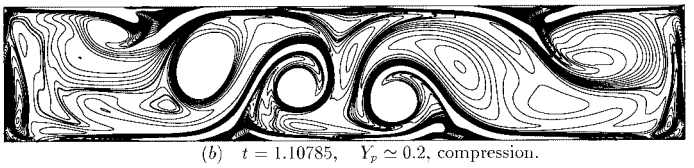

(b) $t = 1.10785$, $Y_p \simeq 0.2$, compression.

(c) $t = 1.41372$, $Y_p \simeq 0.1$, end of the compression.

Figure 14. Isovorticity lines at various times of the compression of Taylor–Green vortices.

8. CONCLUSION

A common criticism imposed on the spectral methods is that their application should be restricted to a limited class of well-behaved flows, otherwise their accuracy is lost. We have tried to show in this work how these methods can be employed to accurately compute flows for which these methods seem, at first, not well suited. The subtraction technique can be employed to solve a large class of singular flows, where the singularities are associated with non-homogeneous boundary conditions, and for which the leading part of the singular expansion can be constructed analytically. In the case of homogeneous boundary conditions, an algorithm for the computation of the non-determined constants involved in the singular expansion has been associated to the subtraction method. This algorithm takes advantage of the global polynomial approximation of the spectral methods for evaluating the solution near the singular points, where the asymptotic solution is dominant.

The study of the accuracy of the method that has been performed for the driven cavity flow shows that the Chebyshev-collocation method handles corner singularities with an accuracy that is, although not exponential, still of high order. The convergence rates measured in the global L_w^2 norm have proved to be connected with the empirical estimates obtained in Section 2. This investigation allows us to connect in a practical sense the accuracy of the Chebyshev-collocation method to the regularity of the solution. Moreover, the study of the local accuracy has shown that the largest errors are located along the boundaries and that the accuracy observed in the largest part of the domain is higher than the global convergence rate suggests.

Although satisfactory, the result obtained for the injection problem are nevertheless not as good as in the driven cavity. It is to be reminded that the asymptotic analysis shows that this application was much more singular than the driven cavity flow. A domain decomposition method, which locates the singular points at corners of the computational domain as it is done in Reference [10], would allow advantage to be taken of the doubling of the convergence rate observed for corner singularities.

These results do not exhibit the theoretical 'infinite' accuracy commonly associated to spectral methods. Nevertheless, the numerical tests performed for model singular problems show that, as for the Chebyshev-collocation method, the accuracy of high-order finite difference methods is also diminished by the singularities. In particular, spectral methods give better results than a sixth-order Hermitian scheme on a variable mesh, for comparable computational costs.

The use of the third-order projection scheme in association with the NS2 subtraction technique proves to be efficient for computing high-Reynolds number singular flows, such as the periodic flow in the driven cavity or the compressed flow in the piston engine. The calculation of the latter flow, given the complexity of the problem, shows that this method may be promising for problems of engineering interest in realistic situations, such as the three-dimensional flow in a cylindrical piston engine.

ACKNOWLEDGMENTS

The calculations of the piston engine flow have been performed on the Cray C-90 of the IDRIS National Computing Centre (Orsay, France).

REFERENCES

1. Moffatt HK. Viscous and resistive eddies near a sharp corner. *Journal of Fluid Mechanics* 1964; **18**: 1–18.
2. Taylor GI. On scraping viscous fluid from a plane surface. In *Miszellaneen der Angewandten Mechanik (Fetschrift Walter Tollmien)*, Schäfer M (ed.). Akademie-Verlag: Berlin, 1962; 313–315.
3. Burggraf OR. Analytical and numerical studies of the structure of steady separated flows. *Journal of Fluid Mechanics* 1966; **24**: 113–151.
4. Hansen EB, Kelmanson MA. An integral equation justification of the boundary conditions of the driven cavity problem. *Computers and Fluids* 1994; **26**(1): 225–240.
5. Ladevèze J, Peyret R. Calcul numérique d'une solution avec singularité des équations de Navier–Stokes: écoulement dans un canal avec variation brusque de section. *Journal de Mécanique* 1973; **13**: 367–396.
6. Georgiou GC, Olson LG, Schultz WW. The integrated singular basis function method for the stick-slip and the die-swell problems. *International Journal for Numerical Methods in Fluids* 1991; **13**: 1251–1265.
7. Holstein H, Paddon DJ. A finite difference strategy for re-entrant corner flow. In *Numerical Methods for Fluid Dynamics*, Morton KW, Baines MJ (eds). Academic Press: London, 1982; 341–358.
8. Ma H, Ruth DW. A new scheme for vorticity computations near a sharp corner. *Computers and Fluids* 1994; **23**: 23–38.
9. Chénier E, Delcarte C, Labrosse G. Stability of the axisymmetric buoyant-capillary flows in a laterally heated liquid bridge. *Physics of Fluids* 1999; **11**: 527–541.
10. Raspo I, Ouazzani J, Peyret R. A spectral multidomain technique for the computation of the Czochralski melt configuration. *International Journal for Numerical Methods in Heat and Fluid Flow* 1996; **6**: 31–58.
11. Hancock C, Lewis E, Moffatt HK. Effects of inertia in forced corner flows. *Journal of Fluid Mechanics* 1981; **112**: 315–327.
12. Kondrat'ev VA. Asymptotic solution of the Navier–Stokes equations near the angular point of the boundary. *Prikladnaya Matematika i Mekhanika (Journal of Applied Mathematics and Mechanics)* 1967; **31**: 119–123.
13. Fix G, Gulatti S, Wakoff GI. On the use of singular functions with finite element approximations. *Journal of Computational Physics* 1973; **13**: 209–238.
14. Georgiou GC, Schultz WW, Olson LG. Singular finite elements for the sudden-expansion and the die-well problems. *International Journal for Numerical Methods in Fluids* 1990; **10**: 357–372.
15. Schönauer W, Weiss R, Gebhard B. Singularity-adapted difference formulas on body-oriented grids. *Zeitschrift für Angewandte Mathematik und Mechanik* 1990; **70**: T654–T656.
16. Maders H, Demay Y, Agassant JF. Numerical and analytical study of the stress singularity in an isothermal Newtonian Stokes flow in a plane convergent geometry. *European Journal of Mechanics, B/Fluids* 1990; **9**: 75–92.
17. Floryan JM, Czechowski L. On the numerical treatment of corner singularity in the vorticity field. *Journal of Computational Physics* 1995; **118**: 222–228.
18. Schumack MR, Schultz WW, Boyd JP. Spectral method solution of the Stokes equations on nonstaggered grids. *Journal of Computational Physics* 1991; **94**: 30–58.
19. Schultz WW, Lee NY, Boyd JP. Chebyshev pseudospectral method of viscous flow with corner singularities. *Journal of Scientific Computing* 1989; **4**: 1–24.
20. Botella O. On the solution of the Navier–Stokes equations using Chebyshev projection schemes with third-order accuracy in time. *Computers and Fluids* 1997; **26**: 107–116.
21. Botella O, Peyret R. The Chebyshev approximation for the solution of singular Navier–Stokes problems. In *Proceedings of the Third Summer Conference on Numerical Modelling in Continuum Mechanics*, Feistauer M, Rannacher R, Kozel K (eds). Matfyzpress: Prague, 1998; 81–90.
22. Botella O, Peyret R. Benchmark spectral results on the lid-driven cavity flow. *Computers and Fluids* 1998; **27**: 421–433.
23. Bernardi C, Maday Y. *Approximations Spectrales de Problèmes oux Limites Elliptiques*. Springer: Paris, 1992.
24. Quarteroni A, Valli A. *Numerical Approximation of Partial Differential Equations*. Springer: Berlin, 1994.
25. Bernardi C, Maday Y. Polynomial approximation of some singular functions. *Applicable Analysis* 1991; **42**: 1–32.
26. Canuto C, Hussaini MY, Quarteroni A, Zang TA. *Spectral Methods in Fluid Dynamics*. Springer: New York, 1988.
27. Peyret R, Taylor TD. *Computational Methods for Fluid Flow*. Springer: New York, 1983.
28. Botella O. Résolution numérique de problèmes de Navier–Stokes singuliers par une méthode de projection Tchebychev. Doctorate thesis, Université de Nice–Sophia Antipolis, 1998.
29. Canuto C, Quarteroni A. Variational methods in the theoretical analysis of spectral approximations. In *Spectral Methods for Partial Differential Equations*, Voigt RG, Gottlieb D, Hussaini MY (eds). SIAM-CBMS: Philadelphia, PA, 1984; 55–78.

30. Pathria D, Karniadakis GE. Spectral element methods for elliptic problems in nonsmooth domains. *Journal of Computational Physics* 1995; **122**: 83–95.
31. Babuška I, Suri M. The p and h–p versions of the finite element method, basic principles and properties. *SIAM Review* 1994; **36**: 578–632.
32. Batchelor GK. *An Introduction to Fluid Dynamics*. Cambridge University Press: Cambridge, 1967.
33. Gupta MM, Manohar RP, Noble B. Nature of viscous flows near sharp corners. *Computers and Fluids* 1981; **9**: 379–388.
34. Ehrenstein U, Peyret R. A Chebyshev-collocation method for the Navier–Stokes equations with application to double-diffusive convection. *International Journal for Numerical Methods in Fluids* 1989; **9**: 427–452.
35. Gear GW. *Numerical Initial Value Problems in Ordinary Differential Equations*. Prentice Hall: Englewood Cliffs, NJ, 1971.
36. Heywood JC, Rannacher R. Finite element approximation of the nonstationary Navier–Stokes problem. I: regularity of the solutions and second-order error estimates for spatial discretization. *SIAM Journal of Numerical Analysis* 1982; **19**: 275–311.
37. Temam R. Behaviour at time $t = 0$ of the solutions of semi-linear evolution equations. *Journal of Differential Equations* 1982; **43**: 73–92.
38. Marion M, Temam R. Navier–Stokes equations: theory and approximation. In *Handbook of Numerical Analysis*, vol. VI, Ciarlet PG, Lions JL (eds). Elsevier: Amsterdam, 1998; 503–688.
39. Poliashenko M, Aidun CK. A direct method for computation of simple bifurcations. *Journal of Computational Physics* 1995; **121**: 246–260.
40. Moffatt HK, Duffy BR. Local similarity solutions and their limitations. *Journal of Fluid Mechanics* 1980; **96**: 299–313.
41. Grisvard P. *Elliptic Problems in Non-Smooth Domains*. Pitman: London, 1985.
42. Naitoh K, Takagi Y, Kuwuhara K, Krause E, Ishii K. Three-dimensional computation of transition to turbulence in a reciprocating engine. AIAA Paper, 89-1886, 1989.
43. Güntsch E, Friedrich R. Direct numerical simulation of turbulence compressed in a cylinder. In *Flow Simulations with High-performance Computers II*, Hirschel EH (ed.). Vieweg: Braunschweig, 1996; 213–226.
44. Pascal H, Buffat M. Large eddy simulations of turbulent flows compressed and/or sheared between two walls on parallel computer using a 'divergence-free spectral Galerkin method'. In *Proceedings of the 3rd ECCOMAS Computational Fluid Dynamics Conference*, Désidéri J-A, Hirsch C, Le Tallec P, Pandolfi M, Périaux J (eds). Wiley: Chichester, 1996; 884–891.
45. Lagerstrom PA. Laminar flow theory. In *Theory of Laminar Flows*, Moore FK (ed.). Princeton University Press: Princeton, NJ, 1964; 20–282.

